Irregular activity arises as a natural consequence of synaptic inhibition

D. Terman, J. E. Rubin, and C. O. Diekman

Citation: Chaos: An Interdisciplinary Journal of Nonlinear Science **23**, 046110 (2013); doi: 10.1063/1.4831752
View online: http://dx.doi.org/10.1063/1.4831752
View Table of Contents: http://scitation.aip.org/content/aip/journal/chaos/23/4?ver=pdfcov
Published by the AIP Publishing

Irregular activity arises as a natural consequence of synaptic inhibition

D. Terman,[1,a)] J. E. Rubin,[2,b)] and C. O. Diekman[3,c)]
[1]Department of Mathematics, The Ohio State University, Columbus, Ohio 43210, USA
[2]Department of Mathematics, University of Pittsburgh, Pittsburgh, Pennsylvania 15260, USA
[3]Department of Mathematical Sciences, New Jersey Institute of Technology, Newark, New Jersey 07102, USA

(Received 31 May 2013; accepted 4 November 2013; published online 20 November 2013)

Irregular neuronal activity is observed in a variety of brain regions and states. This work illustrates a novel mechanism by which irregular activity naturally emerges in two-cell neuronal networks featuring coupling by synaptic inhibition. We introduce a one-dimensional map that captures the irregular activity occurring in our simulations of conductance-based differential equations and mathematically analyze the instability of fixed points corresponding to synchronous and antiphase spiking for this map. We find that the irregular solutions that arise exhibit expansion, contraction, and folding in phase space, as expected in chaotic dynamics. Our analysis shows that these features are produced from the interplay of synaptic inhibition with sodium, potassium, and leak currents in a conductance-based framework and provides precise conditions on parameters that ensure that irregular activity will occur. In particular, the temporal details of spiking dynamics must be present for a model to exhibit this irregularity mechanism and must be considered analytically to capture these effects. © *2013 AIP Publishing LLC*. [http://dx.doi.org/10.1063/1.4831752]

Networks of neurons in the brain are very high-dimensional dynamical systems that can produce correspondingly diverse and complex dynamics. While temporal structure such as synchronization can emerge in the activity of such networks, normal activity in the brain is often irregular, lacking recurrent relationships or correlations in the firing times of different neurons. Past analysis of irregular activity in networks of neurons has relied on a balance of different types of interactions that leads to cancellations of correlations in the limit as network size goes to infinity. Here, we introduce and mathematically analyze a novel mechanism for irregular dynamics. This mechanism does not require many neurons, arising already in a two-neuron model network featuring a form of coupling known as synaptic inhibition, nor does it involve cancellation of interactions between neurons. As we show mathematically, the resulting irregularity emerges naturally from the interplay of standard ionic currents, as well as the inhibitory synaptic current through which neurons interact, during the spikes of membrane potential that constitute neuronal activity. Given its generality, the mechanism we elucidate may be a fundamental feature of inhibitory brain networks exhibiting irregular activity.

I. INTRODUCTION

Normal brain states are often characterized by irregular spiking activity, with little correlation among neurons within particular brain regions. In particular, there are many examples of inhibitory networks that generate such irregular activity. For example, experiments have revealed that, within the inhibitory network in the globus pallidus of the basal ganglia, the spike times across pairs of neurons are rather completely uncorrelated under normal resting conditions.[1–4] Indeed, a hallmark of the parkinsonian state is the replacement of this uncorrelated activity by more correlated firing.[1,2,5–7] Another example is cortical networks in the dorsolateral prefrontal cortex, which have been identified as playing a key role in working memory tasks.[8–10] Experiments have demonstrated that during persistent activity, neurons in this area, including a network of interconnected inhibitory fast-spiking interneurons, exhibit highly irregular firing patterns with a Poisson-like spike time distribution.[11,12] Inhibitory networks also play an important role in other brain regions that exhibit irregular spiking activity, such as thalamic networks involved in the generation of sleep and wake states,[13–16] and the hypothalamic suprachiasmatic nuclei that coordinate circadian (~24-h) rhythms.[17–20] Although there have been numerous theoretical and experimental studies of each of these brain regions, the mechanisms underlying their irregular and/or uncorrelated activity remain poorly understood. In this paper, we present a general mechanism by which highly irregular spike time relations can emerge in a network of neurons coupled with reciprocal synaptic inhibition.

Many works of theoretical neuroscience represent the viewpoint that coupling between a pair of neurons necessarily introduces correlations in their spike times. According to this view, irregularity or asynchronous activity requires some sort of cancellation of positive and negative correlations, such as may arise in what are known as balanced input regimes.[21,22] Much of this theory has been worked out in the limit as network size goes to infinity and in models that do not include the temporal features of spikes.[23–28] In contrast, we show that a two-cell network with reciprocal synaptic inhibition can robustly exhibit irregularity. This activity results from the combined effects of synaptic inhibition and various standard ionic currents. In particular, the temporal dynamics of spiking contribute critically to this irregularity mechanism.

a)Electronic mail: terman@math.ohio-state.edu
b)Electronic mail: jonrubin@pitt.edu
c)Electronic mail: diekman@njit.edu

In this paper, we first consider some ordinary differential equation models for a pair of neurons reciprocally coupled by synaptic inhibition, including two from the literature based on experimental data for particular brain regions.[29,30] We use numerical simulations to illustrate that these generate chaotic dynamics. Next, we define a one-dimensional map for one of these models and demonstrate numerically that the complex dynamics of the full system is very well approximated by the dynamics of this reduced map. We subsequently proceed to analyze properties of the map. First, we show numerically how the map structure relates to changes in the relative timing, and order, of spike firing by the two neurons. Subsequently, we derive analytical estimates on the derivative of the map at points corresponding to both synchronous and antiphase solutions. The analysis leads to rather precise conditions on parameters for when each of these solutions is unstable. The mechanism that we analyze does not require highly specialized or complicated intrinsic dynamics. Our results do, however, depend on properties of the spike itself. Specifically, the effects we consider would not show up in integrate-and-fire type models that neglect the dynamics of spiking and subsequent repolarization. Finally, we consider larger inhibitory networks and use numerical simulations to show that these may also exhibit highly irregular and uncorrelated spiking activity.

II. FROM DIFFERENTIAL EQUATIONS TO A ONE-DIMENSIONAL MAP

A. Basic model equations

Consider the two-cell neural network governed by the equations

$$\begin{aligned} Cv_i' &= -I_{Na}(v_i,n_i) - I_K(v_i,n_i) - I_L(v_i) - I_{syn}(v_i,s_j),\\ n_i' &= \phi(n_\infty(v_i) - n_i)/\tau_n(v_i),\\ s_i' &= \alpha(1-s_i)s_\infty(v_i) - \beta s_i, \end{aligned} \tag{1}$$

for $i \in \{1,2\}, j = 3-i$, where $I_{Na}(v,n) = g_{Na}m_\infty^3(v)(1-n)(v-v_{Na})$, $I_K(v,n) = g_K n^4(v-v_K)$, $I_L = g_L(v-v_L)$, and $I_{syn}(v,s) = g_{syn}s(v-v_{syn})$. The parameter $g_{syn} \geq 0$ and we consider v_{syn} such that $v_i > v_{syn}$ always holds, corresponding to synaptic inhibition. Note that in system (1), the synaptic conductance s_1 depends on v_1 and appears in the I_{syn} term in the differential equation for v_2, and vice versa. In the s_i equation, we assume that $s_\infty(v)$ is an approximation of the Heaviside step function with threshold θ. Additional functions appearing in model (1) are

$$\begin{aligned} m_\infty(v) &= (1+\exp(-(v-\theta_m)/\sigma_m))^{-1},\\ n_\infty(v) &= (1+\exp(-(v-\theta_n)/\sigma_n))^{-1}\\ s_\infty(v) &= (1+\exp(-(v-\theta_s)/\sigma_s))^{-1},\\ \tau_n(v) &= \tau_0 + \tau_1/(1+\exp(-(v-\theta_\tau)/\sigma_\tau)). \end{aligned}$$

Model (1) is a fairly standard conductance-based model, incorporating the basic ionic currents studied by Hodgkin and Huxley.[31] Our default parameter values, which appear in Table I, lie within biologically relevant ranges if we consider them to be given in the units specified in the table; we omit mention of units throughout the remainder of the paper. Note that we chose $v_L = -30$ to mimic the effect of a nonselective cation, since most neurons include additional cationic currents. In fact, our analysis shows that irregular activity becomes more robust for more hyperpolarized values of v_L (e.g., Figure 16).

B. Periodic solutions

For our analysis, we assume that for a single uncoupled cell, defined by $g_{syn} = 0$, the v- and w-nullclines are cubic-shaped and monotone increasing curves, respectively, that intersect at a single point along the middle branch of the v-nullcline. Moreover, $v' > 0 (< 0)$ below (above) the v-nullcline and $w' > 0 (< 0)$ below (above) the w-nullcline. With these assumptions, it is not hard to show that there must be a periodic solution $\Gamma_0 = \{X_0(t) = (v_0(t), n_0(t), s_0(t)) : t \in \mathbb{R}\}$ of the single cell model if the parameter ϕ is sufficiently small. Moreover, there must also exist a synchronous periodic solution of Eq. (1) if the coupling strength g_{syn} is not too large. For g_{syn} fixed at any such value, we denote the synchronous periodic solution as Γ_g, and we will later find conditions on parameters so that Γ_g is unstable.

Figure 1(a) shows the trajectory corresponding to the periodic solution Γ_0 in the phase plane. Note that this trajectory differs from a so-called "relaxation oscillator," which has been used in numerous previous studies of reduced neuronal dynamics.[33] A relaxation oscillator, as shown in Figure 1(b), is usually defined in the limit $\phi \to 0$ and tracks very close to the left and right branches of the cubic-like v-nullcline during the silent and active phases. The jump-up and jump-down between these two phases occur when the trajectory reaches either the left or right fold, or knee, of the cubic-shaped nullcline. Except where $|v'(t)| \approx 0$ when the trajectory crosses the v-nullcline, $|v'(t)| > 5|n'(t)|$. The periodic solution for system (1) that we consider, on the other hand, does not track close to the left branch of the cubic nullcline during the silent phase. Instead, after the

TABLE I. Parameter values for system (1).

Conductances (nS)	Reversal potentials (mV)	Half activations (mV)	Slopes	Rate constants (1/ms)	Other
$g_{Na} = 100.0$	$v_{Na} = 55.0$	$\theta_m = -37.0$	$\sigma_m = 10.0$	$\phi = 0.2$	$C = 1.0$ pF
$g_K = 10.0$	$v_K = -80.0$	$\theta_n = -50.0$	$\sigma_n = 14.0$	$\alpha = 5.0$	$\tau_0 = 0.05$ ms
$g_{syn} = 0.2$	$v_{syn} = -100.0$	$\theta_s = -30.0$	$\sigma_s = 0.1$	$\beta = 1.0$	$\tau_1 = 0.27$ ms
$g_L = 0.02$	$v_L = -30.0$	$\theta_\tau = -40.0$	$\sigma_\tau = -12.0$		

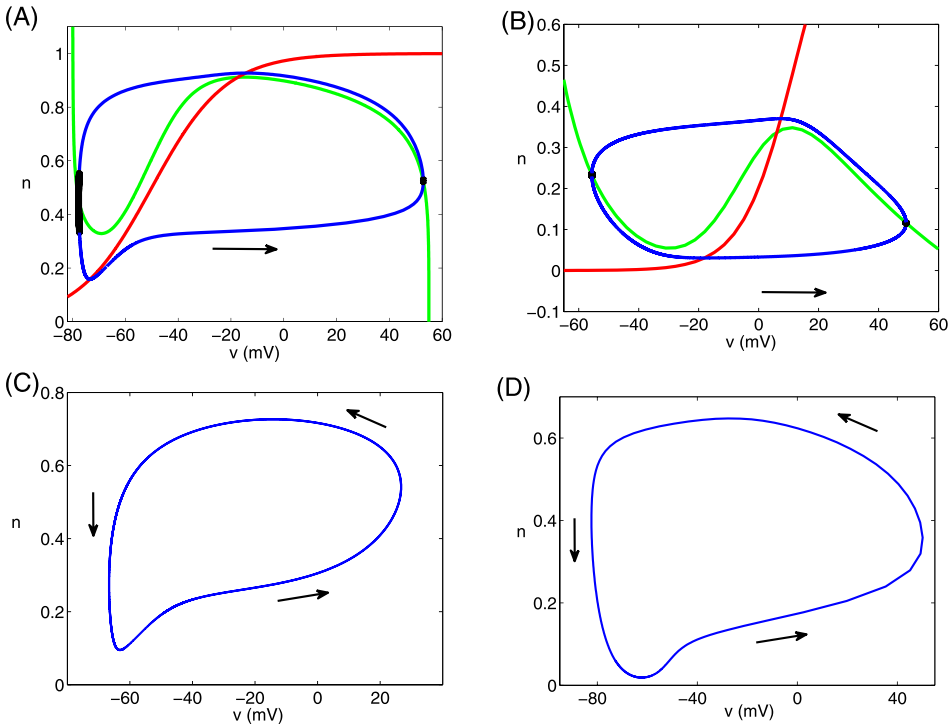

FIG. 1. Nullclines and periodic solutions for single neuron models. (a) Model (1) with $g_{syn}=0$. (b) Relaxation oscillation in the standard Morris-Lecar model (Ref. 32, with parameters tuned to the Type I regime). In both cases, the v-nullcline appears in green, the n-nullcline in red, and a periodic solution in blue and black. Each periodic solution is colored black where $|v'(t)| < 5|n'(t)|$ and blue elsewhere. (c) Projection of periodic solution for the Wang-Buzsaki model.[29] (D) Projection of periodic solution for the Destexhe-Paré model.[30] XPPAUT codes for the Morris-Lecar, Wang-Buzsaki, and Destexhe-Paré models can be found at the website: http://www.math.pitt.edu/~bard/bardware/neurobook/allodes.html.

jump down from the active phase (i.e., termination of a spike), the trajectory quickly moves nearly vertically, with $|v'(t)| < 5|n'(t)|$ much of the time, until it crosses the n-nullcline. After this crossing, it tracks close to the n-nullcline until $v \approx -60$, which is close to spike threshold, above which the trajectory jumps back up to the active phase. As we shall see, this difference in the geometry of the periodic solutions has a profound impact on the dynamics of the coupled cell network.

We note that several well-known models for neuronal activity exhibit phase plane dynamics qualitatively similar to what we show in Figure 1(a). These include the Wang-Buzsaki model for hippocampal interneurons[29] and the Destexhe-Paré model for neocortical pyramidal neurons.[30] In Figures 1(c) and 1(d), we show projections of a periodic solution of each of these models onto the (v,n) phase plane.

C. Two coupled cells generate chaotic activity that is captured by a one-dimensional map

The dynamics of model (1) depends on the strength of the coupling parameter g_{syn}. Figure 2 shows solutions of the model for different values of g_{syn}. Numerical simulations demonstrate that the model exhibits stable synchrony for $g_{syn} < 0.14$ and what appears to be chaotic dynamics for $0.14 < g_{syn} < 0.49$. Such apparently chaotic solutions are shown in Figures 2(b) and 2(c). Note that as g_{syn} increases in this range, each cell tends to fire on more consecutive cycles, while the other cell remains silent. For $g_{syn} > 0.49$, the model exhibits a so-called *suppressed solution* in which one cell fires periodically and the other cell remains silent. Such a solution is shown in Figure 2(d).

Figure 3(a) shows another example of the time courses of v_1, v_2 for a solution of the model (1) with $g_{syn}=0.2$. Note that the two cells fire in a very irregular manner. They often take turns firing, but sometimes a cell fires two consecutive spikes before the other one fires. To demonstrate the irregularity of this solution more definitively, we compute a map as follows. We fix v_1^* within the range of subthreshold v values. We then integrate the model with a random initial condition. After discarding a long transient, we record data each time that $v_1(t) = v_1^*$ with $v_1'(t) > 0$. Suppose that these section crossings take place at times $\{\hat{t}_k\}$. We define a subsequence, call it $\{t_k\}$, of $\{\hat{t}_k\}$ by keeping the times between which cell 1 spikes (defined by the condition that n_1 increases through 0.5). We plot the points $(v_2(t_k), v_2(t_{k+1}))$, generated using $v_1^* = -67$, in blue in Figure 3(b). Note that the resulting points seem to fill out an entire curve, which corresponds to a chaotic attractor of the system. Moreover, the derivative of this curve has absolute value greater than one, except near the curve's local maximum and minimum. This is another indication of chaotic behavior.[34,35] In fact, the trajectory has a positive Lyapunov exponent, 0.0481, as computed using the Gram-Schmidt reorthonormalization procedure implemented in MATDS.[36,37]

We define another one-dimensional map that is more amenable to mathematical analysis, which we refer to as the reduced map, as follows. First, we simulate model (1) with $g_{syn}=0$ to collect coordinates of a dense mesh of points on the periodic solution Γ_0. Denote these points as $\{(v^k, n^k)\}$. We then consider model (1) with $g_{syn} > 0$. For each k, we integrate (1) with cell 1 always starting from the point on Γ_0 with $v_1 = -67$ and $v_1' > 0$ $(v_1 = -67,\ n_1 = 0.2066,\ s_1 = 0)$ and with initial conditions for cell 2 at $(v_2, n_2, s_2) = (v^k, n^k, 0)$. We then record the v_2 value at the time τ_k that we select such that $v_1(\tau_k) = -67, v_1'(\tau_k) > 0$ and cell 1 fires exactly one spike for $0 < t < \tau_k$. Finally, we plot a curve that interpolates the points $(v^k, v_2(\tau_k))$; this curve is shown in

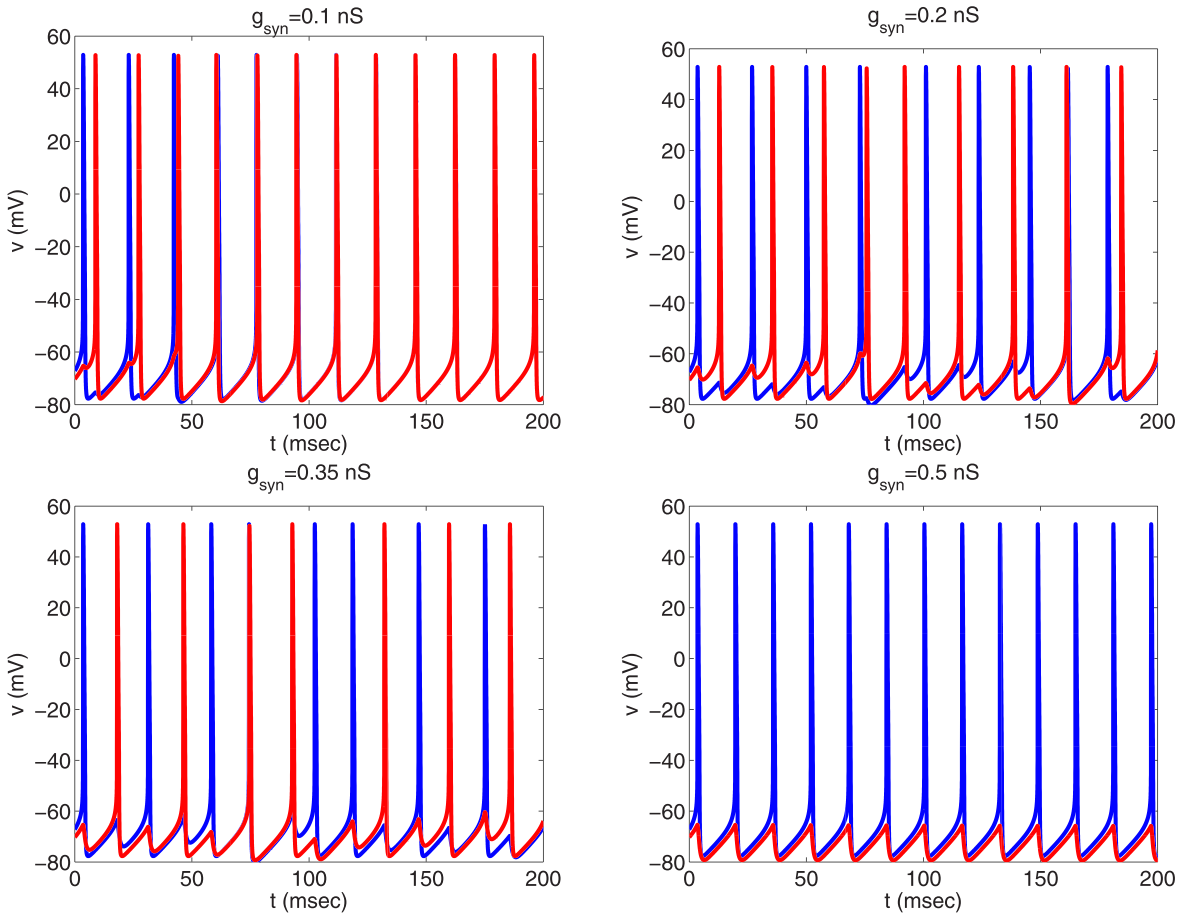

FIG. 2. Dependence on g_{syn}. The synchronous solution is stable for $g_{syn} = 0.1$, but the model exhibits chaotic oscillations for $g_{syn} = 0.2$ and 0.35. If $g_{syn} = 0.5$, then there is a suppressed solution in which one cell fires continuously, while the other cell is silent.

Figure 3(c), and it is presented together with the blue curve from Figure 3(b) in Figure 3(d). We observe that the attractor of the full model—that is, the blue curve in Figure 3B or 3D—is very well approximated by the attractor of the reduced map. This is, in some sense, not surprising because the projections of solutions of Eq. (1) with $g_{syn} > 0$, small, onto the (v,n) plane lie very close to the periodic trajectory Γ_0. We further note that the reduced map has two fixed points, both of which are unstable. The fixed point at $v_2 = -67$ corresponds to the synchronous solution.

Since the singular solution is a closed orbit, the one-dimensional map is, in fact, a map of a topological circle. To each value of v_2 in the map's domain there correspond two points on the singular solution (except at the two "endpoints"): one in which $v_2' > 0$, corresponding to the interval between spikes, and another with $v_2' < 0$, corresponding the spiking phase. We are primarily interested in the points where $v_2' > 0$, since these will contain the global attractor. However, it may happen that $v_2' < 0$ when v_1 hits its section, especially if the crossing occurs when v_2 has recently fired a spike. In Figure 3(c), the part of the black curve generated from initial conditions with $v_2'(0) < 0$ is solid, while the rest is dashed. There is a sharp, nearly vertical portion of the dashed black curve at $v^k \approx -73$ where the map appears to be discontinuous. This corresponds to points v^k that are mapped to points $v_2(\tau_k)$ such that $v_2'(\tau_k) < 0$. We note that this vertical portion of the black curve crosses the identity line $v_2(\tau_k) = v^k$. However, this does not correspond to a fixed point of the map since v^k lies on the portion of Γ_0 where $v' > 0$, while $v_2(\tau_k)$ lies near the portion of Γ_0 where $v' < 0$.

Note that in the free-running simulation used to generate Figure 3(b), no such points are represented; that is, it appears to be extremely unlikely that cell 2 will have just fired a spike when v_1 increases through -67 after a cell 1 spike. For other section choices, however, we can encounter such points. An example of such a reduced map appears in Figure 4, generated from taking a section at $v_1^* = -50$ (i.e., resetting to $v_1 = -50, n_1 = 0.3135, s_1 = 0$ on Γ_0). From this starting point, an uncoupled cell has $v' > 0$ and will quickly approach spike threshold. The discrete points (blue and red) in Figure 4(a) were generated analogously to those in Figure 3(b), while the continuous curve (black solid and dashed) in Figure 4(b) was produced the same way as that in Figure 3(c). The red points, however, feature $v_2'(t_k) < 0$, which did not arise in Figure 3(b). We find that if $v_2'(t_k) < 0$, then it always follows that $v_2'(t_{k+1}) > 1$. Thus, points from intervals where the slope has smaller magnitude map to the intervals where the curve is steep. These numerics suggest that further consideration of a section at $v_1^* = -50$ will be particularly revealing about how the cells can switch spiking order. Thus, in the next subsection, we perform some additional numerical explorations using this section, to elucidate how the

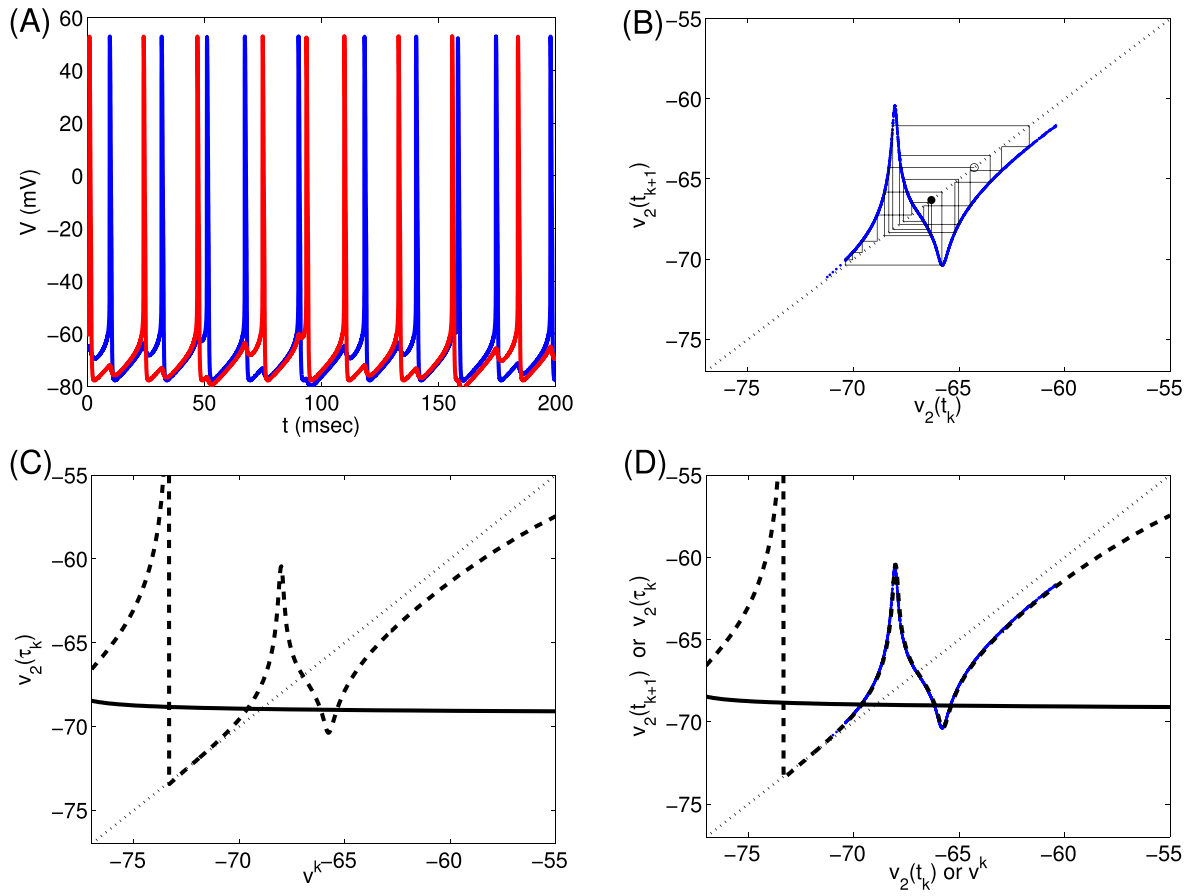

FIG. 3. Numerical evidence of irregular activity from the model (1) with $g_{syn} = 0.2$. (a) Time courses of v_1 (blue) and v_2 (red) from random initial conditions. (b) $v_2(t_{k+1})$ versus $v_2(t_k)$, where $\{t_k\}$ are defined by the conditions $v_1(t_k) = -67$, $v_1'(t_k) > 0$, and v_1 fires exactly one spike on (t_k, t_{k+1}), from a free-running simulation of 5×10^4 msec starting from random initial conditions. The cobwebbing segment was selected randomly from within a run after a transient was discarded. It starts and ends at the v_2 values indicated by the black and open dots, respectively. The black dotted curve is the identity line. (c) Similar data to (b), generated using repeated simulations of initial conditions along Γ_0 ($v_2(\tau_k)$ versus v^k; see text). The dashed (solid) part of the black curve corresponds to $v_2' > 0$ ($v_2' < 0$) when cell 1 crosses the section at -67 (the curve is closed but parts above $v = -55$ and below $v = -77$ are cut off here to focus on the central features). (d) Superposition of the curves from (b) and (c).

structure of the reduced map emerges from changes in the timing and order of the two neurons' spikes.

Figure 5 shows additional examples of the full map corresponding to three different values of g_{syn}. Note that the absolute value of the derivative of the map at $v^k = -67$ is less than one if $g_{syn} = 0.1$, but is greater than one if $g_{syn} = 0.2$ or 0.5. Hence, the synchronous solution is stable for $g_{syn} = 0.1$ but unstable for $g_{syn} = 0.2$ and 0.5. Further note

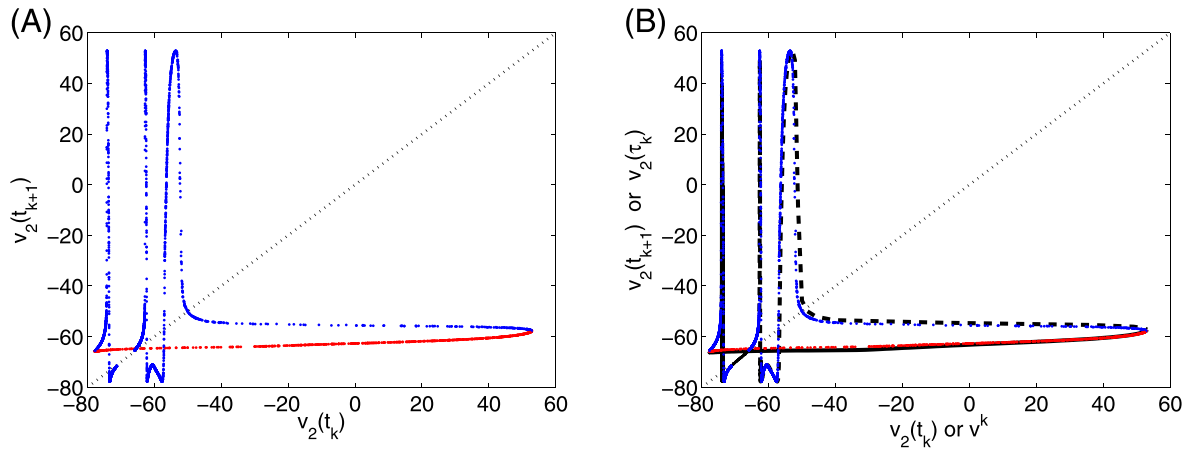

FIG. 4. Mapping of v_2 values across successive times when $v_1 = -50$ with $v_1' > 0$, from the reduced model (1) with $g_{syn} = 0.2$. (a) Discrete points show $v_2(t_{k+1})$ versus $v_2(t_k)$ from a free-running simulation of 5×10^4 ms starting from random initial conditions, similar to Figure 3(b). Points are colored blue (red) if $v_2'(t_k) > 0$ ($v_2'(t_k) < 0$). (b) Superimposed on the data from (a) is a continuous curve that interpolates points generated using repeated simulations of initial conditions along Γ_0, similar to Figures 3(c) and 3(d). The black solid (dashed) part of the curve corresponds to $v_2' > 0$ ($v_2' < 0$) when cell 1 crosses the section.

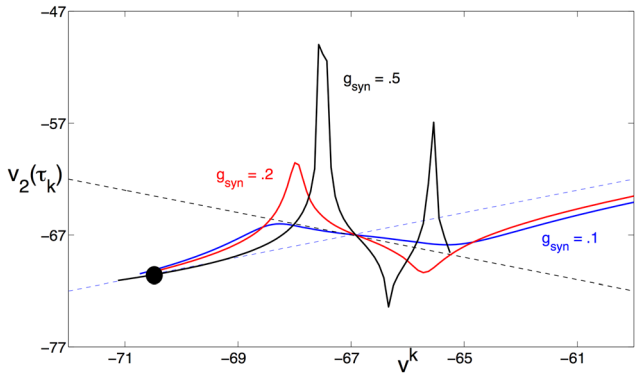

FIG. 5. The full map for $g_{syn} = 0.1$ (blue), 0.2 (red), and 0.5. The synchronous solution, corresponding the fixed point at $(-67, -67)$, is stable for $g_{syn} = 0.1$ but unstable for $g_{syn} = 0.2$ and 0.5. There is a stable fixed point, indicated by the black circle, when $g_{syn} = 0.5$ corresponding to a suppressed solution.

that there is a stable fixed point, indicated by the black circle, when $g_{syn} = 0.5$. This fixed point corresponds to the suppressed solution.

We note that there does not exist a stable antiphase solution for any value of g_{syn}. However, stable antiphase solutions can emerge if we change some other model parameter. For example, if $\sigma_m = 9$, then stable antiphase solutions exist for $0 < g_{syn} < 0.4$. In fact, the model is bistable for $0 < g_{syn} < 0.1$. Over this range of g_{syn}, there exist both a stable synchronous solution and a stable antiphase solution. Further discussion of the antiphase solution is given later.

To define the one dimensional reduced map, we need to assume that the synaptic variables s_1 and s_2 decay very close to zero during consecutive action potentials of the corresponding neuron. This decay occurs if the parameter β, corresponding to the synaptic decay rate, is sufficiently large. For the simulations, we chose $\beta = 1.0\, msec^{-1}$. However, experiments have demonstrated that inhibitory $GABA_A$ synapses decay at a rate that is about 10 times slower. In Figure 6, we computed the full map for the model with $\beta = 0.18\, msec^{-1}$ and $g_{syn} = 0.09$. Note that the solution is chaotic; however, the dynamics can no longer be captured by a reduced one-dimensional map. This simplification is not possible because we can no longer assume

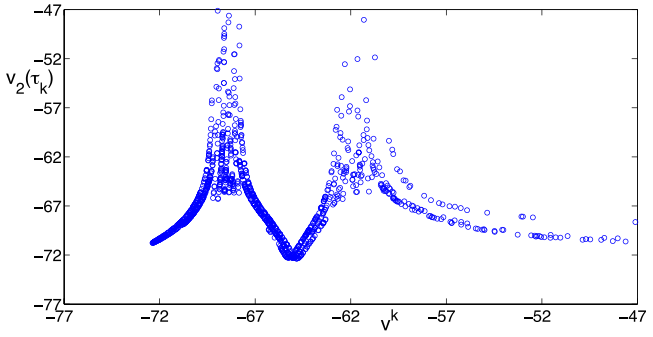

FIG. 6. The full map for $\beta = 0.18$.

that the synaptic variables are zero when defining the reduced map. So, in fact, more complicated dynamics may come into play when considering more realistic, slower synaptic dynamics.

Finally, we note that the full map for each of the Wang-Buzsaki and Destexhe-Paré models, as shown in Figure 7, has a qualitatively similar structure to that of model (1). In particular, this map consists of regions where the slope has magnitude greater than one interrupted by abrupt deviations or discontinuities. Consistent with the analysis developed in this paper, networks formed from neurons described by either model, coupled through synaptic inhibition, can exhibit irregular dynamics.[38,39]

III. NUMERICAL ANALYSIS OF MAP STRUCTURE

To gain insight about the dynamics of model (1) and the source of the structure of the reduced map, we replot the data from the curve in Figure 4 generated from the section $v_1^* = -50$. Recall that each iterate starts at time 0, and the kth iterate ends at time τ_k. We now plot $v_2(0) - v_1(0)$ and $v_2(\tau_k) - v_1(\tau_k)$ versus our iteration step number k (which we refer to as a time-like variable, since the initial sampling of points from Γ_0 was based on integration with a uniform time step). The results of this replotting appear in the center of Figure 8. The blue curve denotes $v_2(0) - v_1(0)$ while the green is $v_2(\tau_k) - v_1(\tau_k)$. Along the latter curve, various points are marked with asterisks and numbers. These points

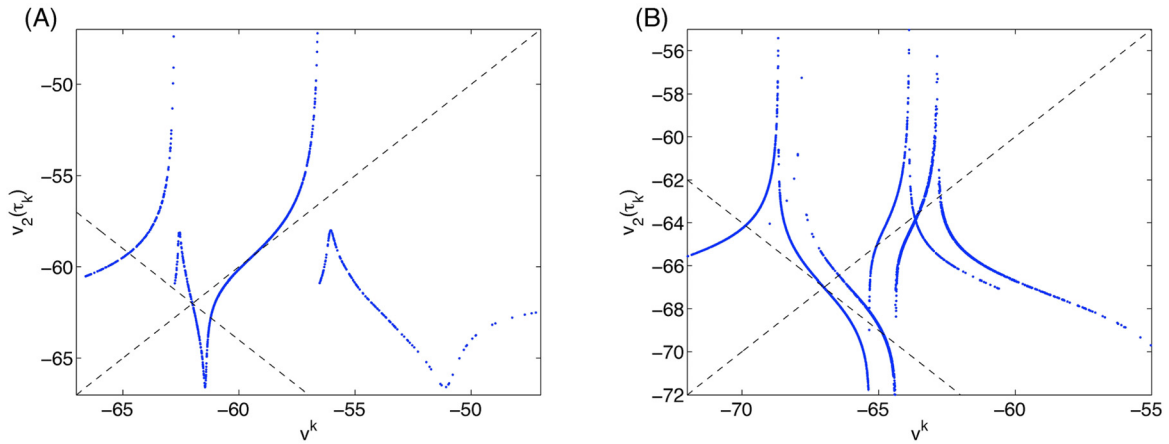

FIG. 7. Iterates of the full map described in this paper, but generated from (left) the Wang-Buzsaki model[29] and (right) the Destexhe-Paré model.[30] Here, we computed the map by first discarding a 10 s transient and then running the models for another 50 s.

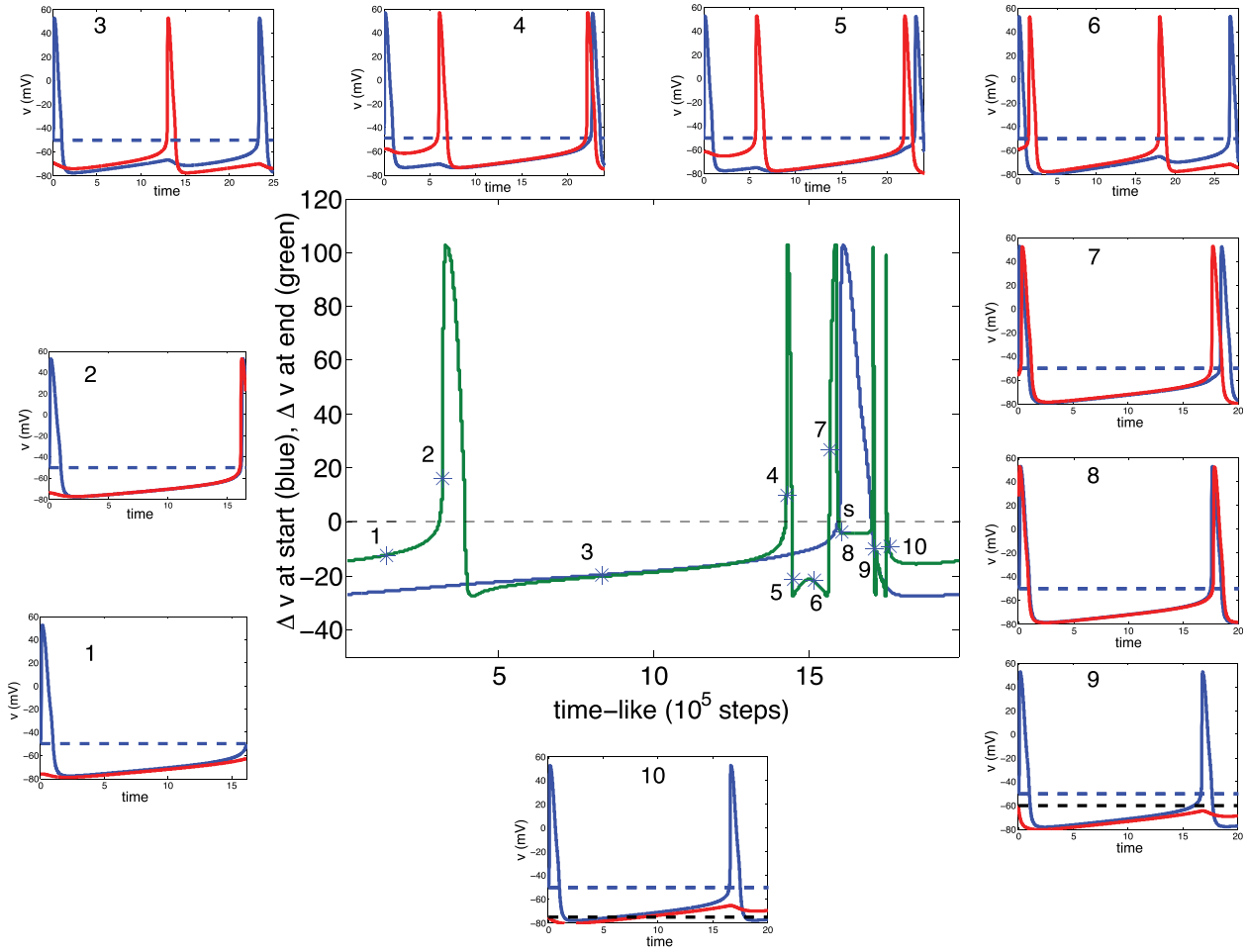

FIG. 8. The return map for a section at $v = -50$. See text for a full description.

label iterates that were selected to represent different regimes that we discuss below. The time courses of v_1 and v_2 from time 0 up to some time greater than or equal to τ_k (chosen to best illustrate each regime) are shown for the numbered iterates in correspondingly numbered panels around the outside of the figure. Possible fixed points, namely states in which v_2 always takes the same value whenever $v_1 = -50$ with $v_1' > 0$, arise at iterates where the blue and green curves coincide. In reality, however, most of these coincidences turn out to be cases where $v_2(\tau_k) = v_2(0)$ but $v_2'(0) > 0$ and $v_2'(\tau_k) < 0$; that is, v_2 ends up on the "opposite side" of the orbit from where it starts. The actual synchronous fixed point occurs near point 8, where the blue and green curves together cross the dashed line at 0 and is labeled with an 's'. We will now discuss the various regimes that occur within the simulation.

In regime 1, represented by the leftmost asterisk in Figure 8 (center) and the panel numbered "1," cell 2 starts significantly "behind" cell 1, with v_2 much farther below spike threshold than v_1. Due to this disadvantage, the inhibition to cell 2 that results from the spike of cell 1 allows cell 1 to overtake cell 2 after spiking. Thus, when $v_1(\tau_k) = -50$ for $\tau_k > 0$ with $v_1'(\tau_k) > 0$, we still have $v_2(\tau_k) < -50$, but $v_2(\tau_k) > v_2(0)$ and thus the green curve lies above the blue in this regime. This regime ends where the green curve hits 0, which represents an iterate such that v_2 manages to first reach -50 at exactly the time that v_1 returns there.

In regime 2, cell 2 spikes before v_1 reaches -50, but it does not have time to complete its spike before this happens. In the panel numbered "2," for example, the two cells' trajectories cross $\{v = -50\}$, just after time 15, so close together in time that we cannot distinguish them; nonetheless, because the voltage traces are so steep at threshold crossing, $v_2 - v_1$ is almost 20 when this happens (point 2 in Figure 8, center). This regime can be viewed as ending when the green curve next hits 0 (with negative slope). At the iterate where that occurs, $v_2(\tau_k) = -50$ with $v_2'(\tau_k) < 0$: cell 2 and cell 1 have the same voltage at time τ_k but cell 2 is finishing its spike while cell 1 approaches spike threshold. Similarly, the point between "2" and "3" where the blue and green curves intersect is not a true fixed point for the same reason.

The regime represented by point 3 in Figure 8 (center) is a simple one in which cell 2 does manage to spike after cell 1 and is still quite far below spike threshold, in its recovery phase, when $v_1(\tau_k) = -50$ with $v_1'(\tau_k) > 0$ occurs. This is a long phase in terms of iterates, because the rate of change of voltage well below spike threshold is relatively small and there is a significant interval of $v_2(0)$ values over which this regime occurs. There is a fixed point corresponding to a form of antiphase spiking within this regime, quite close to point 3, yet numerically we see that it is weakly unstable, due to the greater slope of the green curve than the blue one there.

The positive slope of the green curve in regime 3 means that as we progress through this regime, the ending value of v_2 increases; note that cell 2 spikes progressively earlier, which is what yields the larger final values. If cell 2 spikes earlier, then it inhibits cell 1 earlier, and in this model, this earlier inhibition produces a longer delay before cell 1 can return to spike threshold. Eventually, when $v_2(0)$ is large enough, it can manage to overtake cell 1 and fire a second spike before cell 1 can spike again. The transition to this case occurs at the third 0 crossing of the green curve in Figure 8 (center). Point 4 illustrates what happens beyond this transition as cell 2 achieves its second spike before cell 1, yielding a large $v_2(\tau_k)$.

Continuing this trend, as $v_2(0)$ increases still more and cell 2 spikes still earlier, we observe iterates on which cell 2 is finishing its second spike when cell 1 reaches $v_1 = -50$. By the iterate corresponding to point 5, cell 2 has completed its second spike and fallen well below threshold when $v_1 = -50$, such that the green curve ends up well below the blue one. The intersection between blue and green curves between points 4 and 5 is not a true fixed point; analogously to the intersection between points 2 and 3, $v_2'(\tau_k) < 0$ at the iterate at which this intersection occurs.

From point 5 to point 6, the green curve is nonmonotonic, reflecting subtle changes in the effects of inhibition between the two cells. In regime 5, the delay in spiking of cell 1 is due to the inhibition associated with the first spike of cell 2, whereas the second spike of cell 2 has little impact. In regime 6, the opposite holds, as it is the second spike of cell 2 that delays the spiking of cell 1 (see outer panels of Figure 8). Somewhat paradoxically, as cell 2 continues to fire its first spike progressively earlier beyond point 6, this spike continues to impact cell 1 less, and the subsequent spike of cell 1 becomes earlier. Eventually, as represented by point 7, even the second spike of cell 2 cannot delay the second spike of cell 1, and cell 1 spikes while cell 2 is still active. (As previously, the intersection of curves between points 6 and 7 is not a fixed point, due to $v_2'(\tau_k) < 0$.)

After regime 7, we finally reach $v_2(0) = -50$, the fixed point corresponding to the synchronous state. The steep slopes of the curves here suggest that this true fixed point will be unstable, and we will analyze this claim in the next section. Beyond the fixed point is a regime with $v_2(0) > -50$ (blue curve above 0). Here, cell 2 fires its first spike before cell 1, but cell 1 fires its second spike slightly before cell 2, such that the green curve lies below 0, as at point 8. As the initial condition for cell 2 progresses through various points within the spike, with $v_2(0) > -50$, $v_2(\tau_k)$ ends up at roughly the same value as it did for point 8. Once $v_2(0)$ becomes less than -50, with $v_2'(0) < 0$, as represented by point 9, $v_2(\tau_k)$ appears to briefly become much more sensitive to $v_2(0)$; indeed, there may be some numerical inaccuracies in the green curve in this regime. At point 9 and over an interval to its right, at least, the situation is clear: cell 2 is initially in its after-spike hyperpolarization phase, with $v_2'(0) < 0$, and the inhibition from cell 1 helps keep $v_2(t) < v_2(0)$ for all $t > 0$ until v_1 reaches -50 with $v_2(\tau_k) \approx v_2(0)$. Similarly to several previous cases, the condition $v_2'(0) < 0$ prevents fixed points in this regime, even if the blue and green curves intersect.

Finally, for sufficiently negative $v_2(0)$, we return to initial states with $v_2'(0)$ near 0 or positive. As illustrated at point 10, however, the inhibition from cell 1 manages to prevent cell 2 from spiking before the time τ_k such that $v_1(\tau_k) = -50$. Since $v_2'(0)$ is sufficiently close to 0 or positive, we do get $v_2(\tau_k) > v_2(0)$ in this regime, and in fact the situation matches up with regime 1, as it should due to the periodicity of the relevant solutions.

In summary, the numerical experiment illustrated in Figure 8 suggests that as we progress across iterates corresponding to points on Γ_0, over broad intervals, the value of v_2 at our stopping condition varies more rapidly than the value of v_2 at the starting point (green curve versus blue curve). The abrupt variations in the reduced map are linked to the spiking of cell 2, since $v_2(\tau_k)$ is sensitive to $v_2(0)$ when cell 2 spikes near time τ_k. This sensitivity is compounded near switches in the order of spike firing, since both cells' voltages change quickly when both cells are close to threshold at the same time, as occurs near such switches. There appear to be several starting configurations that map to $v_2(\tau_k) = v_1(\tau_k)$ or to $v_2(\tau_k) = v_2(0)$, but for many of these, $v_2'(\tau_k) < 0$, whereas $v_1'(\tau_k) > 0$ by construction, so these configurations do not promote phase-locked states. There do seem to be two true fixed points, one corresponding to synchrony ('s') and the other, near point 3, to an antiphase state, but both appear numerically to be unstable. In Sec. IV, we analytically establish conditions on parameters that ensure the instability of the synchronous state.

IV. INSTABILITY OF THE SYNCHRONOUS STATE

A. The return map Π

Our numerics have revealed a form of sensitivity to initial conditions in system (1), related to the inhibitory interactions between the cells. We now wish to find precise conditions on parameters for when the synchronous solution is unstable. This is done by constructing a one-dimensional map, similar to the maps computed numerically in the previous sections, and then computing the derivative of this map at a point corresponding to the synchronous solution. To define the map, let $X_i(t) = (v_i, n_i, s_i)$ for $i = 1,2$ denote the trajectories corresponding to the two cells. Here, we consider initial conditions so that both $X_1(0)$ and $X_2(0)$ lie on Γ_0 and assume that $s_\infty(v) = H(v - \theta)$ where H is the Heaviside step function. For our analysis, we will make use of various additional notation as illustrated in Figure 9. Fix some $V_0 < \theta$, to be chosen later, and assume that $v_1(0) = V_0$ with $v_1'(0) > 0$. Furthermore, assume that $|v_2(0) - V_0|$ is small with $v_2'(0) > 0$ and choose Δt so that $v_2(\Delta t) = V_0$. (Note that $\Delta t < 0$ if $v_2(0) > V_0$.) The quantity Δt corresponds to the distance between the cells in the "time metric." Now, there must exist a first time $T_0 > 0$ so that $v_1(T_0) = V_0$ and $v_1'(T_0) > 0$. We choose $\widetilde{\Delta t}$ as the minimal in magnitude time so that $v_2(T_0 + \widetilde{\Delta t}) = V_0$ (Figure 9), and we define the map $\Pi : \Delta t \to \widetilde{\Delta t}$.

Note that the synchronous solution corresponds to a fixed point of the map and the synchronous solution is unstable if $|\Pi'(0)| > 1$. In what follows, we find precise conditions for this instability. These conditions are found by following the

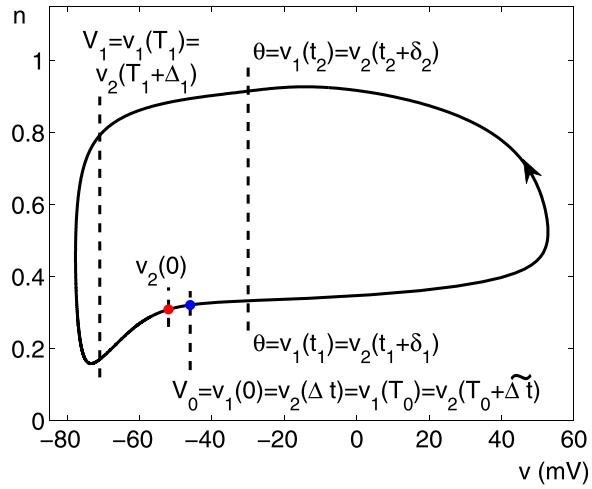

FIG. 9. Set-up for the analysis of the map Π_1. The black solid curve is the periodic orbit Γ_0, generated numerically from model (1) with $g_{syn}=0$. Dashed lines are placed at particular v values used in the proof. The solid blue and red dots provide example starting locations for cell 1 and cell 2, respectively.

trajectories corresponding to the two cells around in phase space and writing Π as the composition of other maps, each corresponding to passage of the solution through some portion of phase space. We make this decomposition because, as we shall see, different components of the model, including both synaptic and intrinsic properties of the cells, control the expansion of solutions within different regions of phase space. Specifically, we write $\Pi = \Pi_3 \circ \Pi_2 \circ \Pi_1$, where

$$\Pi_1 : \Delta t \to \Delta s, \quad \Pi_2 : \Delta s \to \Delta v, \quad \Pi_3 : \Delta v \to \widetilde{\Delta t}.$$

Each map component Π_i is defined and analyzed in a subsection below. We henceforth assume that $v_2(0) < v_1(0)$ so that $\Delta t > 0$. The case $\Delta t < 0$ is similar.

B. The map Π_1

We will use Π_1 to compare the values of the synaptic conductance impacting each cell at the time when its trajectory intersects a section $\{v = V_1\}$, with $V_1 < \min\{v_1(0), v_2(0)\} = v_2(0)$ (Figure 9); in our numerical examples, we take $V_1 = -71$. Specifically, let T_1 and Δ_1 be the smallest positive times so that $v_1(T_1) = v_2(T_1 + \Delta_1) = V_1$. Then $\Pi_1(\Delta t) = \Delta s := s_1(T_1 + \Delta_1) - s_2(T_1)$.

To estimate Δs, let $t_1 < t_2$ be the smallest positive times so that $v_1(t_1) = v_1(t_2) = \theta$, and let $\delta_1 < \delta_2$ be the smallest positive times so that $v_2(t_1 + \delta_1) = v_2(t_2 + \delta_2) = \theta$ (Figure 9). Then

$$s_1' = \begin{cases} \alpha(1 - s_1), & t_1 < t < t_2, \\ -\beta s_1, & 0 < t < t_1, \quad t_2 < t < T_1 + \Delta_1, \end{cases}$$

$$s_2' = \begin{cases} \alpha(1 - s_2), & t_1 + \delta_1 < t < t_2 + \delta_2, \\ -\beta s_2, & 0 < t < t_1 + \delta_1, \quad t_2 + \delta_2 < t < T_1. \end{cases}$$

We assume that $s_1(0) = s_2(0) = 0$, which is a good approximation if β is sufficiently large relative to the duration of the interspike interval of the synchronous solution.

Note that if $g_{syn} = 0$, then $X_1(t)$ and $X_2(t)$ both lie on the same synchronous solution and the "time metric" between the two cells remains invariant; hence, $\delta_1 = \delta_2 = \Delta_1 = \Delta t$. We claim that if $g_{syn} > 0$ is small, then one can still approximate δ_1, δ_2 and Δ_1 by Δt. In brief, this is because during this "spiking" phase of the solution, the synaptic currents are dominated by the Na^+ and K^+ ionic currents. Hence, coupling due to the synaptic currents has little effect on the trajectories corresponding to the two cells. More precisely, we note that during a spike, when $v > \theta$, we can approximate the nonlinear functions $m_\infty(v)$ and $n_\infty(v)$ by 1. Assuming further that $\tau_n(v)$ is constant, we can approximate the first two equations in Eq. (1) by the linear system

$$\begin{aligned} Cv_i' &= -g_{Na}(1 - n_i)(v_i - v_{Na}) - g_K n_i^4 (v_i - v_K) \\ &\quad - g_L(v_i - v_L) - g_{syn} s_j (v_i - v_{syn}), \\ n_i' &= k(1 - n_i). \end{aligned} \tag{2}$$

Now consider δ_1, the time it takes v_2 to travel from $v_2(t_1)$ to θ. Without synaptic input, this time would be Δt. Hence, the ratio $\delta_1/\Delta t$ is, to first order in Δt, equal to the ratio of v' without synaptic input to v' with synaptic input, evaluated at the point along Γ_0 with $v = \theta$. For our default parameters, we find that $\delta_1 \approx (1.004)\Delta t$.

To estimate δ_2 and Δ_1, we solve the linear system (2) explicitly for different initial conditions corresponding to the two cells. Note that

$$n_i(t) = 1 + (n_i(0) - 1)e^{-kt}$$

and the solution of the first equation in Eq. (2) can be written as the sum of four functions, each the solution of a differential equation corresponding to one of the four terms on the right hand side of Eq. (2). For example, let (u_1,n_1) and (u_2,n_2) be solutions of the linear system

$$\begin{aligned} Cu' &= -g_{Na}(1 - n)(u - v_{Na}), \\ n' &= k(1 - n), \end{aligned} \tag{3}$$

where $u_1(0) = u_2(0) = \theta$ and $n_1(0) \neq n_2(0)$. Note that the solution of the first equation in Eq. (3) is given by

$$u(t) = v_{Na} + (\theta - v_{Na})\exp\left\{-\frac{g_{Na}}{k}(1 - n(0))(1 - e^{-kt})\right\}.$$

Hence,

$$\begin{aligned} |u_1(t) - u_2(t)| &= (v_{Na} - \theta)\exp\left\{-\frac{g_{Na}}{Ck}(1 - n_1(0))(1 - e^{-kt})\right\} \\ &\quad \times \left[1 - \exp\left\{-\frac{g_{Na}}{Ck}|n_2(0) - n_1(0)|(1 - e^{-kt})\right\}\right] \\ &\approx (v_{Na} - \theta)\exp\left\{-\frac{g_{Na}}{Ck}(1 - n_1(0))(1 - e^{-kt})\right\} \\ &\quad \times \frac{g_{Na}}{Ck}|n_2(0) - n_1(0)|(1 - e^{-kt}) \\ &< \frac{g_{Na}(v_{Na} - \theta)}{Ck} e^{-g_{Na}/2Ck} |n_1(0) - n_2(0)|, \end{aligned} \tag{4}$$

using the fact that $|n_1(0) - n_2(0)|$ is small for perturbations from synchrony and assuming that $(1 - n_1(0))(1 - e^{-kt}) > 1/2$, as we observe numerically. For our default parameters, we have that $g_{Na}/Ck \approx 25$, from which it follows that there is a huge amount of compression. In a similar way we can estimate compression of the other three solutions of the linear equations corresponding to the other terms on the right hand side of Eq. (2). Based on this compression, we conclude that there is little change in the time metric distance between cells while their voltages exceed θ and hence δ_2 and Δ_1 can be very closely approximated by δ_1, which we have shown is closely approximated by Δt.

If we let $M_1 = t_2 - t_1$ and $M_2 = T_1 - t_2$, then these approximations yield

$$s_1(T_1 + \Delta_1) \approx (1 - e^{-\alpha M_1})e^{-\beta(M_2+\Delta t)},$$
$$s_2(T_1) \approx (1 - e^{-\alpha M_1})e^{-\beta(M_2-\Delta t)}$$

so that

$$\Pi_1(\Delta t) \approx (1 - e^{-\alpha M_1})e^{-\beta M_2}(e^{-\beta\Delta t} - e^{\beta\Delta t}).$$

Thus,

$$\Pi_1'(0) \approx -2\beta e^{-\beta M_2} \tag{5}$$

in the limit $\alpha \gg 1$. Numerically, for our default parameters and $\theta = -30$, the passage time $M_2 \approx 0.36$ and $\Pi_1'(0) \approx -1.4$. The negative sign of $\Pi_1'(0)$ implies that if $v_1(0) > v_2(0)$, then cell 1 is more inhibited when it reaches $\{v = V_1\}$ than is cell 2 when it reaches the same section.

Finally, note that $n_1(T_1) > n_2(T_1 + \Delta_1)$. This relation holds because, as shown in Figure 10, the trajectory corresponding to cell 2 lies "inside" that of cell 1. More precisely, for $0 < t < t_1$, the cells are essentially uncoupled and evolve along the synchronous solution. The synaptic variable s_1 activates when $t = t_1$, while s_2 does not activate until $t = t_1 + \delta_1$. Hence, for $t_1 < t < t_1 + \delta_1$, the vectors $(v_2'(t), n_2'(t))$ have greater slope than $(v_1'(t), n_1'(t))$. During this time, cell 1 remains on the synchronous solution, while cell 2 is "pushed inside" of the synchronous solution by a small amount. An example of this effect is illustrated in Figure 10(a). The blue curve is a segment of Γ_0. The black curve points in the direction of (v_1', n_1') evaluated at the initial point of the segment at

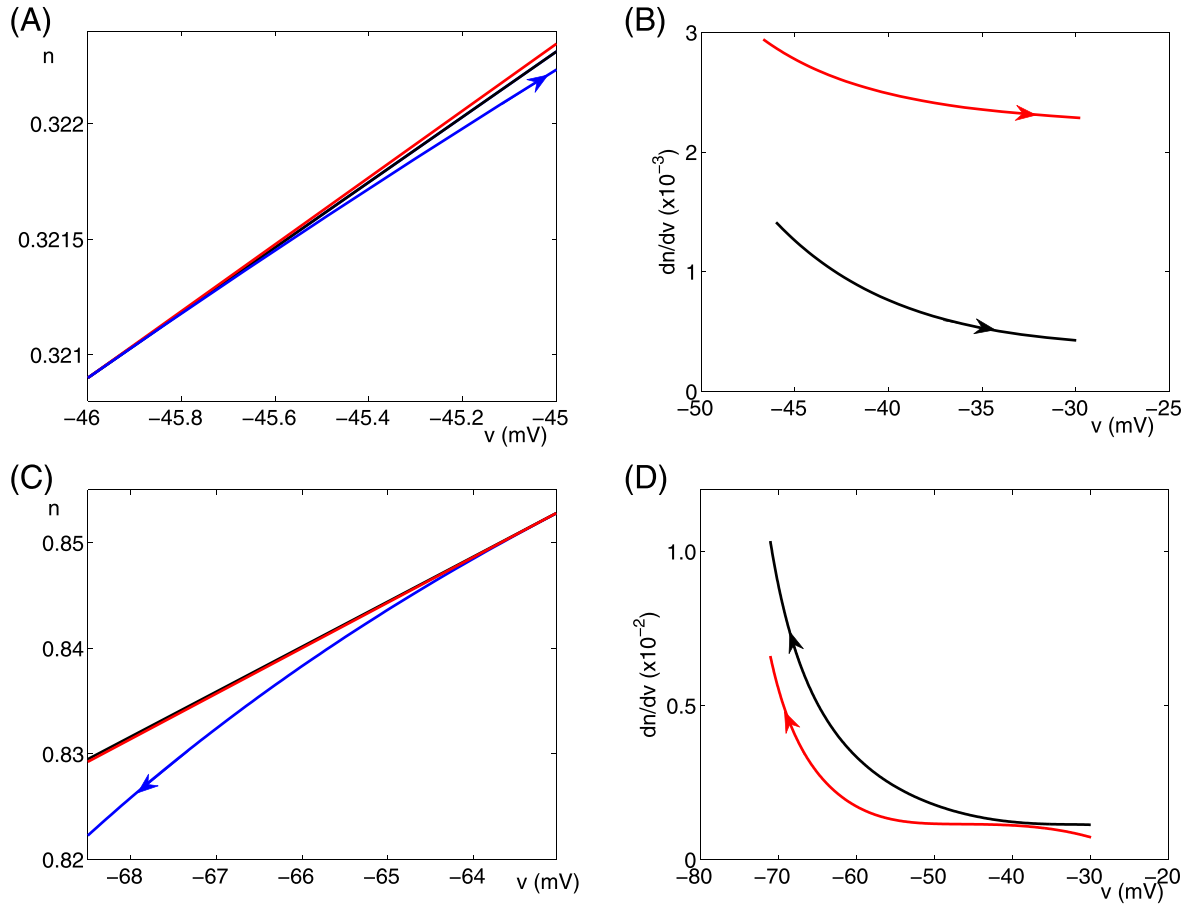

FIG. 10. Numerical illustration that the trajectory of cell 2 ends up inside that of cell 1 during the Π_1 phase of the orbit of system (1). (a) For a particular point on Γ_0 (blue) with $v = -46$, the black segment points in the direction of (v_1', n_1'). The red segment similarly points in the direction of (v_2', n_2') when $v_2 = -46$ (although cell 2 is not on Γ_0 at that time because $s_1 > 0$) and lies "inside" of the black segment. (b) dn/dv versus v for cell 1 (black) and cell 2 (red) along the solution of (1) considered from $v = -46$ until the voltages increase through the synaptic threshold $\theta = -30$. Along these curves, $v_i', n_i' > 0$ for both i, and $dn_2/dv_2 > dn_1/dv_1$. (c) Structures analogous to (a) but generated at a much later time, when each cell reaches $v = -63$ after firing a spike (and neither cell is on Γ_0). When cell 2 attains $v_2 = -63$, s_1 is much smaller than s_2 was when $v_1 = -63$, which causes the segment for cell 2 to point inside that for cell 1 again (i.e., towards smaller n). (d) Analogous to (b), but with curves occurring from the time the voltages decrease through θ to the end of the regime where Π_1 is defined, at $v = -71$. Along these curves, $v_i', n_i' < 0$ for both i, and $dn_2/dv_2 < dn_1/dv_1$.

the time when cell 1 reaches this point. Similarly, the red curve points in the direction of (v_2', n_2') when v_2 reaches the voltage coordinate of that point, at which time $s_1 > 0$. From Figure 10(b), we see that the relation $dn_2/dv_2 > dn_1/dv_1$ holds for voltages all the way up to the threshold $\theta = -30$. Subsequently, for $t_1 + \delta < t < t_2$, both cells receive synaptic input and satisfy essentially the same system of equations. (Here, we are assuming that $\alpha \gg 1$ so that when activated, $s_1 \approx s_2 \approx 1$.) Since (v_1, n_1) and (v_2, n_2) satisfy the same system of equations, cell 2's trajectory must remain inside that of cell 1. Finally, s_1 deactivates at $t = t_2$, while s_2 deactivates later at $t = t_2 + \delta_2$. Hence, $s_1(t) < s_2(t)$ for $t_2 < t < T_1 + \Delta_1$. It follows that during this time the vectors $(v_2'(t), n_2'(t))$ have more negative slope than $(v_1'(t), n_1'(t))$ and the trajectory corresponding to cell 2 remains inside that of cell 1. This effect is shown in Figure 10(c), which is analogous to Figure 10(a) but is computed at a sub-threshold voltage after spike firing, and in Figure 10(d), which is analogous to Figure 10(b) but is computed from the times when the cells' voltages decrease through θ to the end of the regime where Π_1 is defined. In summary, we have explained why $n_1 > n_2$ at the points where the trajectories cross the section $\{v = V_1\}$; that is, why $n_a := n_1(T_1) > n_b := n_2(T_1 + \Delta_1)$.

C. The map Π_2

For the next map component Π_2, we start from $\{v = V_1\}$, such that the composition $\Pi_2 \circ \Pi_1$ is well-defined, and track each trajectory until it crosses a section $\{n = N_2\}$ for an appropriately chosen $N_2 < n_b$. That is, $\Pi_2(\Delta s) = v_1(T_{12}) - v_2(T_{22}) := \Delta v$ where, for $i = 1$ or 2, $T_{i2} = \min\{t > 0 : n_i(T_{i2}) = N_2, n_i'(T_{i2}) < 0\}$. Here, it will be convenient to translate time so that both trajectories, $(v_1(t), n_1(t))$ and $(v_2(t), n_2(t))$, begin on the section $\{v = V_1\}$. Let $s_a = s_1(T_1 + \Delta_1)$ and $s_b = s_2(T_1)$. Now, if we translate time by T_1, then based on the notation from the previous subsection, the trajectory for cell 1 has initial condition $(v_1(0), n_1(0)) = (V_1, n_a)$, and cell 1 is subject to exponentially decaying inhibition from cell 2 with $s_2(0) = s_b$. Similarly, if we translate time by $T_1 + \Delta_1$, then the trajectory for cell 2 has initial condition $(v_2(0), n_2(0)) = (V_1, n_b)$, and cell 2 is subject to exponentially decaying inhibition from cell 1 with $s_1(0) = s_a$. In both cases, we abuse notation and denote the translated time by t. Although $t = 0$ refers to different times for the different trajectories, the map Π_2 will take $\Delta s = s_a - s_b < 0$ to a value Δv, and hence the particular times at which the trajectories are generated are irrelevant, given that we have incorporated the appropriate starting values of the s_i.

We make some assumptions to simplify the analysis that follows. First, we ignore I_{Na}, since we are considering the subthreshold portion of the trajectory where $m_\infty(v)$, and therefore I_{Na}, is very small. We also assume that for this range of v, both $n_\infty(v)$ and $\tau_n(v)$ are constant. We can then write the differential equation for each n_i as

$$n' = k(a - n),$$

where a and k are positive constants. Hence, both $n_1(t)$ and $n_2(t)$ satisfy

$$n(t) = a + (n(0) - a)e^{-kt}, \tag{6}$$

with $n_1(0) = n_a$ and $n_2(0) = n_b$ and with $n_a > n_b$ from the previous subsection. In addition to requiring that our stopping section $\{n = N_2\}$ satisfies $N_2 < n_b$, we henceforth take $N_2 > a$.

Denote the curves $(v_1(t), n_1(t))$ and $(v_2(t), n_2(t))$ as $v = \Gamma_1(n)$ and $v = \Gamma_2(n)$, respectively. As shown in Figure 11, we construct a curve $v = \Psi_{\Delta s}(n)$, for $N_2 \le n \le n_b$, so that $\Psi_{\Delta s}(n_b) = V_1$, $\Psi_{\Delta s} < \Gamma_2$ for $n < n_b$, and along $\Psi_{\Delta s}$, the vector field corresponding to cell 1 points towards the left, away from Γ_2. That is,

$$v' - n'\Psi_{\Delta s}'(n) < 0. \tag{7}$$

This last condition, together with the fact that $n_1(0) = n_a > n_b$, implies that the curve $\{v = \Gamma_1(n)\}$ lies "outside" of $\{v = \Psi_{\Delta s}(n)\}$, with $v_1(n) < v_2(n)$ for each $n \in [N_2, n_b]$, as shown in Figure 11. This relation allows us to estimate

$$\Pi_2(\Delta s) = \Gamma_2(N_2) - \Gamma_1(N_2) > \Gamma_2(N_2) - \Psi_{\Delta s}(N_2). \tag{8}$$

We write $\Psi_{\Delta s}(n) = \Gamma_2(n) - \Lambda_{\Delta s}(n)$ where $\Lambda_{\Delta s}(n_b) = 0$ and $\Lambda_{\Delta s}(n) > 0$ for $N_2 \le n < n_b$. Then along $v = \Psi_{\Delta s}(n)$, the vector field corresponding to cell 1 satisfies

$$\begin{aligned} v' &= -g_L(v - v_L) - g_K n^4(v - v_K) - g_{syn}s_2(v - v_{syn}) \\ &= -g_L(\Gamma_2(n) - v_L) - g_K n^4(\Gamma_2(n) - v_K) \\ &\quad - g_{syn}s_1(\Gamma_2(n) - v_{syn}) \\ &\quad + g_L\Lambda_{\Delta s}(n) + g_K n^4\Lambda_{\Delta s}(n) + g_{syn}s_1\Lambda_{\Delta s}(n) \\ &\quad + g_{syn}\Delta s e^{-\beta t}(\Gamma_2(n) - v_{syn}) \\ &= n'\Gamma_2'(n) + \left[g_L + g_{syn}s_1(t) + g_K n^4\right]\Lambda_{\Delta s}(n) \\ &\quad + g_{syn}\Delta s e^{-\beta t}B(n) \end{aligned}$$

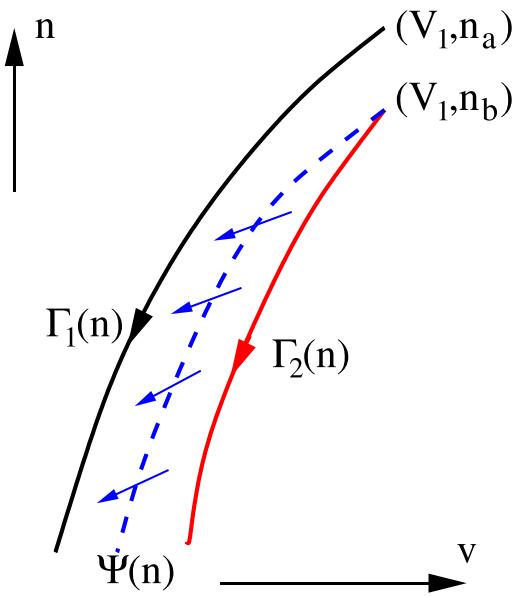

FIG. 11. Schematic illustration of the definition and use of the curve $v = \Psi_{\Delta s}(n)$ (subscript omitted below and in the figure for convenience). The trajectory for cell 2 (red, $\{v = \Gamma_2(n)\}$) lies inside that of cell 1 (black, $\{v = \Gamma_1(n)\}$) at the start of the analysis of Π_2, at $v = V_1$. The curve $\{v = \Psi(n)\}$ (blue dashed) emanates from (V_1, n_b) and satisfies $\Psi(n) < \Gamma_2(n)$ for all relevant n. The vector field (blue arrows) points to the left of $\{v = \Psi(n)\}$ everywhere on the curve, which implies that $\Gamma_1(n) < \Gamma_2(n)$ for all relevant n.

where $B(n) = \Gamma_2(n) - v_{syn}$. Hence, we need to choose $\Lambda_{\Delta s}(n)$ so that

$$\begin{aligned} 0 > v' - n'\Psi'_{\Delta s}(n) &= v' - n'\Gamma'_2(n) + n'\Lambda'_{\Delta s}(n) \\ &= n'\Lambda'_{\Delta s}(n) + \left[g_L + g_{syn}s_1(t) + g_K n^4\right]\Lambda_{\Delta s}(n) \\ &\quad + g_{syn}\Delta s e^{-\beta t}B(n). \end{aligned}$$

Note that Eq. (6) implies that

$$e^{-\beta t} = \left(\frac{n-a}{n_b-a}\right)^{\lambda} \equiv H_0(n), \tag{9}$$

where

$$\lambda = \beta/k. \tag{10}$$

Since $s_1(t) = s_a e^{-\beta t}$ and $s_a < 1$, it suffices to choose $\Lambda_{\Delta s}(n)$ so that

$$\begin{aligned} &k(a-n)\Lambda'_{\Delta s}(n) + [g_L + g_{syn}H_0(n) + g_k n^4]\Lambda_{\Delta s}(n) \\ &\quad \le g_{syn}\rho H_0(n)B(n). \end{aligned} \tag{11}$$

We consider the *Ansatz*

$$\Lambda_\rho(n) = -M\left[(n_b-a)^{\lambda} - (n-a)^{\lambda}\right]\Delta s > 0 \tag{12}$$

and seek an upper bound on M, such that Eq. (11), and hence Eq. (7), is guaranteed to hold for all M values up to this bound. Plugging the *Ansatz* into Eq. (11) and then dividing by the quantity $(n-a)^{\lambda}$, we obtain

$$M\left\{\beta + [g_L + g_{syn}H_0(n) + g_k n^4]H(n)\right\} \le g_{syn}\widetilde{B}(n), \tag{13}$$

where

$$H(n) = \left(\left[\frac{n_b-a}{n-a}\right]^{\lambda} - 1\right) \quad \text{and} \quad \widetilde{B}(n) = B(n)\left(\frac{1}{n_b-a}\right)^{\lambda}.$$

For $N_2 \le n \le n_b$, let

$$\begin{aligned} &A_1^* = \max\{H(n)\}, \quad A_2^* = \max\{H_0(n)H(n)\}, \\ &A_3^* = \max\{n^4 H(n)\} \quad \text{and} \quad B^* = \min\{\widetilde{B}(n)\}. \end{aligned}$$

We then obtain an upper bound for M:

$$M \le \frac{g_{syn}B^*}{\beta + g_L A_1^* + g_{syn}A_2^* + g_k A_3^*} \equiv M^* \tag{14}$$

and it follows from Eqs. (8), (12), and (14) that

$$|\Pi'_2(0)| > M^*[(n_b-a)^{\lambda} - (N_2-a)^{\lambda}].$$

For the default values in the numerical simulations, we have that $\lambda \approx 1.5$ and $n_b \approx 0.8$. Note that the parameter a approximates $n_\infty(v)$ and during this portion of the trajectory, $a \approx 0.12$. Furthermore, $B(n) = \Gamma_2(n) - v_{syn} > 20$. Finally, we let $N_2 = 0.25$. For these choices of the parameters, we find numerically that

$$A_1^* \approx 11, \quad A_2^* \approx .9, \quad A_3^* \approx .1 \quad \text{and} \quad B^* \approx 35.67. \tag{15}$$

Letting $g_{syn} = .2$, $g_L = .02$, $\beta = 1$ and $g_K = 10$, Eqs. (14) and (15) give the estimate

$$M^* \approx 2.97 \quad \text{and} \quad (n_b-a)^{\lambda} - (N_2-a)^{\lambda} \approx .514.$$

Thus, we estimate that

$$|\Pi'_2(0)| > M^*[(n_b-a)^{\lambda} - (N_2-a)^{\lambda}] \approx 1.53.$$

Note that $\Pi'_2(0)$ is in fact positive; for example, if the cells' synaptic conductances at $\{v = V_1\}$ come closer together such that Δs becomes less negative, then Δv also becomes less negative.

Finally, we need to estimate T_{12} and T_{22}, the (original) times at which the two trajectories cross the section $\{n = N_2\}$. Recall that cells 1 and 2 cross the first section $\{v = V_1\}$ at times T_1 and $T_1 + \Delta_1$, respectively. Let $\hat{T}_2$ be the time of passage of cell 2 from $\{v = V_1\}$ to $\{n = N_2\}$. Then $T_{22} = T_1 + \Delta_1 + \hat{T}_2$. Since $n_b > n_a$, it follows that the time of passage of cell 1 from $\{v = V_1\}$ to $\{n = N_2\}$ is greater than $\hat{T}_2$. Hence, $T_{12} > T_1 + \hat{T}_2$ and, therefore,

$$T_{12} - T_{22} > -\Delta_1 \approx -\Delta t. \tag{16}$$

D. The map Π_3

The map $\Pi_3 : \Delta v \to \widetilde{\Delta t}$ computes the difference in the time of passage for trajectories from two different initial v values in the section $\{n = N_2\}$ to return to the original section $\{v = V_0\}$. For this part of the flow, we assume that the synaptic and potassium currents have decayed away to negligible levels, as seen numerically. We note that during the initial portion of this part of the flow, the sodium current is also still negligible; however, it does begin to activate well before v reaches V_0. We choose $V_3 < V_0$ so that the sodium current is negligible as long as $v < V_3$ and split the analysis into two parts corresponding to before and after the sodium current has begun to activate.

As long as $v < V_3$, v satisfies the equation

$$v' = -g_L(v - v_L). \tag{17}$$

Solving this simple ODE and computing the time of passage from $v = V$ to $v = V_3$ yields

$$t = \frac{1}{g_L}\ln\left(\frac{V - v_L}{V_3 - v_L}\right). \tag{18}$$

Recall that T_{12} and T_{22} denote the times when the two cells' trajectories cross the section $\{n = N_2\}$, respectively. From Eq. (18), it follows that the times at which cells 1 and 2 cross $v = V_3$ are

$$\begin{aligned} T_{13} &= T_{12} + \frac{1}{g_L}\ln\left(\frac{v_1(T_{12}) - v_L}{V_3 - v_L}\right) \quad \text{and} \\ T_{23} &= T_{22} + \frac{1}{g_L}\ln\left(\frac{v_2(T_{22}) - v_L}{V_3 - v_L}\right), \end{aligned}$$

respectively. Hence, using Eq. (16),

$$\begin{aligned} T_{23} - T_{13} &= T_{22} - T_{12} + \frac{1}{g_L}\left[\ln\left(\frac{v_2(T_{22}) - v_L}{V_3 - v_L}\right)\right. \\ &\quad \left. - \ln\left(\frac{v_1(T_{12}) - v_L}{V_3 - v_L}\right)\right] \\ &< \Delta t + \frac{1}{g_L}\left[\ln(v_2(T_{22}) - v_L) - \ln(v_1(T_{12}) - v_L)\right] \\ &\approx \Delta t - \frac{\Delta v}{g_L(v_1(T_{12}) - v_L)}, \end{aligned} \tag{19}$$

where $\Delta v := v_1(T_{12}) - v_2(T_{22}) < 0$ and the denominator in the final expression is negative as well. If we write $\Delta v = m\Delta t$, with $m < 0$ since $\Delta v < 0 < \Delta t$, then we have expansion in the time metric if

$$\Delta t\left(1 - \frac{m}{g_L(v_1(T_{12}) - v_L)}\right) < -\Delta t,$$

or $m < 2g_L(v_1(T_{12}) - v_L) < 0$. From our estimates of $|\Pi_1'(0)|$ and $|\Pi_2'(0)|$, we have $m < -2.14$, whereas for our default parameter values, $2g_L(v_1(T_{12}) - v_L) > -2.04$. Moreover, simulations show that the latter expression becomes closer to 0 much faster than m as we take smaller perturbations from synchrony.

Remark: In our analysis, we neglected some effects that contribute to the numerical results. First, $n_\infty(v)$ is not exactly constant, and its slope decreases T_{12} and hence increases $T_{23} - T_{13}$, which works against expansion. On the other hand, the inhibitory current I_{syn} to cell 1 is larger during the Π_2 phase of the map than is the inhibitory current to cell 2 there, which makes Δv more negative and hence makes $T_{23} - T_{13}$ more negative as well. These effects counteract each other and are quite minor compared to those we maintain in the analysis.

We claim that the time metric between the cells remains very close to invariant as they pass from $\{v = V_3\}$ to $\{v = V_0\}$, completing the cycle. This implies that the expansion is maintained until the cells reach the section $\{v = V_0\}$. To prove our claim, we note that invariance must hold if both (v_1, n_1) and (v_2, n_2) lie on the same trajectory (i.e., if both trajectories cross the section $\{v = V_3\}$ at exactly the same value of n, with negligible synaptic currents). While this last condition is not strictly met, we claim that the two trajectories (v_1, n_1) and (v_2, n_2) do, in fact, converge at an exponential rate to an invariant curve; in particular, the points where they cross $\{v = V_3\}$ are exponentially close to each other.

Choose a value $V_2 < V_3$ such that the trajectories (v_1, n_1) and (v_2, n_2) both cross the section $\{v = V_2\}$ while traveling from $\{n = N_2\}$ to $\{v = V_3\}$. While the two trajectories travel from $\{v = V_2\}$ to $\{v = V_3\}$, both voltage variables satisfy Eq. (17); moreover, the n variables satisfy

$$n' = \phi_n(n_\infty(v) - n)/\tau_n(v). \tag{20}$$

It is not hard to show that two solutions of this last equation with different initial conditions are compressed at an exponential rate depending on the size of $\phi/\tau_n(v)$, as illustrated in an example in Figure 12.

Note that, as defined, the first component of the map evaluated at the synchronous solution has a negative derivative less than -1, while the second and third have positive derivatives greater than 1. For example, a perturbation to the synchronous state that delays the trailing cell's threshold crossing (more positive Δt) causes the lead cell to experience a larger synaptic conductance on return to the silent phase (more negative Δs), causing that cell to drop to more negative voltages (more negative Δv) and fall farther behind the originally trailing cell (more negative $\widetilde{\Delta t}$).

V. EXPANSION AWAY FROM THE SYNCHRONOUS SOLUTION

We now demonstrate that the map Π exhibits expansion for initial points some distance away from the synchronous solution. As before, we consider solutions that begin with both cells along the lower branch of Γ_0 with $v_2(0) < v_1(0) = V_0$. Suppose that the time metric between the cells is Δ; that is, $v_2(\Delta) = V_0$. We will show that $|\Pi'(\Delta)| > 1$ if Δ is not too small or not too big. In particular, our analysis will yield conditions on parameters so that the antiphase solution is unstable.

If Δ is sufficiently large, then cell 2 does not jump up until after cell 1 jumps up and returns to the silent phase. In this case, as shown in Figure 13, when cell 1 does jump up, the resulting inhibition causes cell 2 to "turn around" so that $v_2' < 0$ as long as v_1 is above threshold. Once cell 1 falls below threshold, the inhibition to cell 2 decays and eventually both cells return to near the synchronous trajectory Γ_0 with $v' > 0$. At some later time, cell 2 jumps up and it is now cell 1 that "turns around". When cell 2 falls below threshold, the inhibition to cell 1 decays and both cells return to near Γ_0. We note that if Δ is not too large (e.g., regime 3 in Figure 8), then cell 1 is now ahead of cell 2 along Γ_0 so the cells maintain their orientation after a complete cycle.

Let t_1 denote the time cell 1 crosses the synaptic threshold or fires; that is, $v_1(t_1) = \theta$ and $v_1(t) < \theta$ for $0 < t < t_1$. Note that if there was no inhibition, then cell 2 would cross threshold at time $t_1 + \Delta$. However, because there is inhibition, the

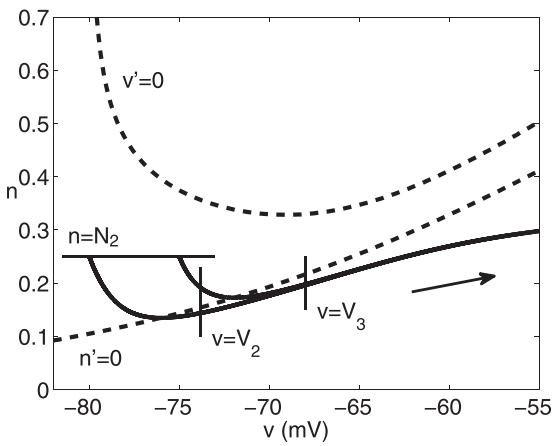

FIG. 12. Compression between two trajectories (solid black curves) of Eq. (1) at the start of the recovery from spiking. The vertical and horizontal line segments represent sections at $\{n = N_2\}$, $\{v = V_2\}$, and $\{v = V_3\}, V_2 < V_3$. The dashed curves are the v- and n-nullclines and the black arrow indicates the direction of flow.

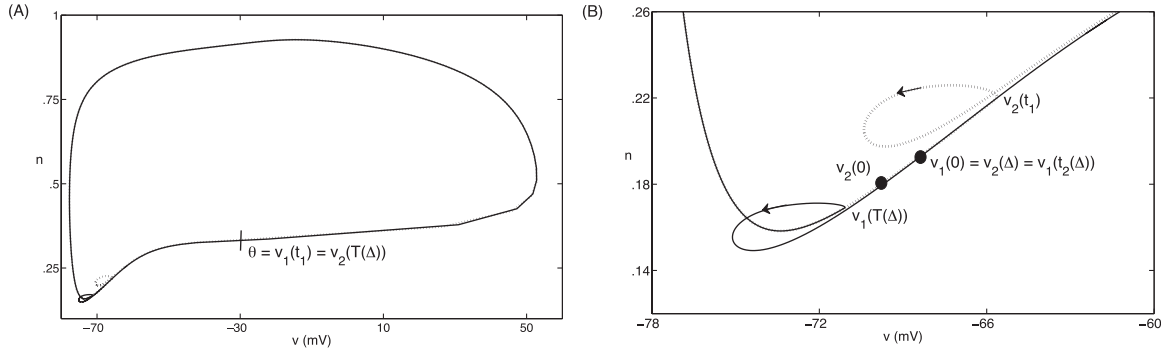

FIG. 13. Projections of the two cells' trajectories onto the (v, n) phase plane. When one cell fires, the other cell "turns around" until the first cell falls below threshold and synaptic input to the other cell decays sufficiently. A blow-up of the lower left region in (a) is shown in (b).

threshold crossing time for cell 2 is delayed. Denote this time as $T(\Delta)$; that is, $v_2(T(\Delta)) = \theta$ and $v_2(t) < \theta$ for $0 < t < T(\Delta)$. A key step in the analysis is the following Lemma, which requires certain conditions on the parameters to be satisfied. In particular, Δ cannot be too large or too small. These conditions are given below.

Lemma 1: $T(\Delta) - \Delta$ is an increasing function of Δ.

Remark: The time at which cell 2 would cross threshold with or without inhibition is $T(\Delta)$ or $t_1 + \Delta$, respectively. Therefore, the Lemma implies that the delay in threshold crossing due to inhibition is an increasing function of Δ.

Proof: Fix $\Delta_a < \Delta_b$ and choose v_a and v_b so that if $v_2(0) = v_a$ or $v_2(0) = v_b$, then the time metric between cell 2 and cell 1 is Δ_a or Δ_b, respectively. We note that $\Delta_a < \Delta_b$ implies that $v_a > v_b$, and the time metric from v_b to v_a is $\Delta_b - \Delta_a$. Let $(v_a(t), n_a(t))$ and $(v_b(t), n_b(t))$ denote the trajectories corresponding to cell 2, with initial conditions that lie along Γ_0 with $v_a(0) = v_a$ and $v_b(0) = v_b$, respectively. (Here, we ignore the synaptic variables, since they are very close to 0).

Until cell 1 fires, at $t = t_1$, both (v_a, n_a) and (v_b, n_b) evolve along the lower branch of Γ_0 and the time metric between them remains invariant. Hence, the time metric from $v_b(t_1)$ to $v_a(t_1)$ is $\Delta_b - \Delta_a$. Once cell 1 fires, however, both (v_a, n_a) and (v_b, n_b) turn around, with both $v_a'(t) < 0$ and $v_b'(t) < 0$ as long as cell 1 remains above threshold. The decrease in v_a and v_b continues until cell 1 falls below threshold. Once the inhibition decays sufficiently, (v_a, n_a) and (v_b, n_b) will turn around again so that both $v_a'(t) > 0$ and $v_b'(t) > 0$. Choose T_a so that $v_a(t) < v_a(t_1)$ for $t_1 < t < T_a$ and $v_a(T_a) = v_a(t_1)$.

We claim that $v_a'(t) > v_b'(t)$ for $t_1 < t < T_a$. Once we prove this claim, the proof of the Lemma follows for the following reason: If $v_a'(t) > v_b'(t)$ for $t_1 < t < T_a$, then

$$v_a(t_1) - v_b(t_1) < v_a(T_a) - v_b(T_a) = v_a(t_1) - v_b(T_a),$$

or $v_b(T_a) < v_b(t_1)$. Since the time metric from $v_b(t_1)$ to $v_a(t_1)$ is $\Delta_b - \Delta_a$, this implies that the time metric from $v_b(T_a)$ to $v_a(T_a)$ is greater than $\Delta_b - \Delta_a$. We assume that for $t > T_a$, the inhibition has decayed sufficiently and both (v_a, n_a) and (v_b, n_b) have returned sufficiently close to Γ_0 so that the time metric from v_b to v_a remains invariant, at least until v_a reaches threshold. From the relative positions of $v_b(T_a)$ and $v_b(t_1)$ and the subsequent time invariance, it follows that

$$T(\Delta_b) - T(\Delta_a) > \Delta_b - \Delta_a \quad \text{or} \quad T(\Delta_b) - \Delta_b > T(\Delta_a) - \Delta_a, \tag{21}$$

which is what we need to show.

To complete the proof of the Lemma, it remains to prove our claim that $v_a'(t) > v_b'(t)$ for $t_1 < t < T_a$. Since $v_a(t_1) > v_b(t_1)$, this inequality follows if we can show that the right hand side of the first equation in Eq. (1) is an increasing function of v. One can interpret this property as saying that the sodium current activates quickly enough. To simplify the analysis somewhat, we ignore the potassium current, since the activation variable n^4 is very small, and assume that n remains roughly constant during the relevant time interval. Let $n_0 = 1 - n$. Then we need that

$$\begin{aligned} 0 &< \frac{\partial}{\partial v}(-I_{Na}(v,n) - I_L(v) - I_{syn}(v,s)) \\ &= 3g_{Na}m_\infty^2(v)m_\infty'(v)n_0(v_{Na} - v) - g_{Na}m_\infty^3(v)n_0 \\ &\quad - g_L - g_{syn}s. \end{aligned} \tag{22}$$

Note that if $m_\infty(v) = (1+\exp(-(v-\theta_m)/\sigma_m))^{-1}$, then $m_\infty'(v) = \exp(-(v-\theta_m)/\sigma_m)m_\infty^2(v)/\sigma_m$. Since $s < 1$, Eq. (22) follows if

$$\begin{aligned} \frac{g_L + g_{syn}}{n_0 g_{Na}} &< m_\infty^3(v) \\ &\quad \times \left(\frac{3}{\sigma_m}\exp(-(v-\theta_m)/\sigma_m)m_\infty(v)(v_{Na} - v) - 1\right). \end{aligned} \tag{23}$$

This last equation gives precise conditions on parameters for when the Lemma holds. For our numerical example, we have that Eq. (23) is satisfied if $-65 < v < -10$. □

We now return to the analysis showing that the map Π exhibits expansion for initial conditions away from the synchronous solution. We continue to use the same notation as in the proof of Lemma 1. Note that while the time t_1 at which cell 1 first reaches threshold does not depend on the initial position of cell 2 – that is, Δ_a or Δ_b – the time at which cell 1 returns to its initial position, on $\{v = V_0\}$, does. We denote this time as $t_2(\Delta_a)$ or $t_2(\Delta_b)$, respectively. Let δ_a and δ_b be the time metric from $v_a(t_2(\Delta_a))$ and $v_b(t_2(\Delta_b))$ to V_0, respectively (Figure 14(a)). Then $\Pi(\Delta_a) = \delta_a$ and $\Pi(\Delta_b) = \delta_b$. We wish to prove the following additional lemma, which will establish the instability of the antiphase solution.

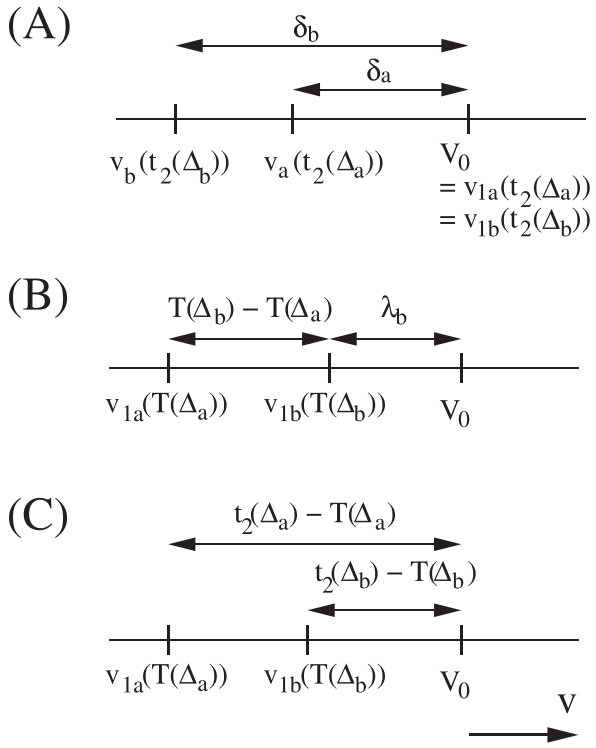

FIG. 14. Voltage values and times used in the proof of Lemma 2, to establish the instability of the antiphase solution. (a) Voltage values and time lags for cell 2 when cell 1 returns to the section $\{v = V_0\}$, depending on the initial time lag Δ_a or Δ_b. (b) Voltage values and times to the section $\{v = V_0\}$ for cell 1 when cell 2 reaches threshold, in the absence of inhibition, depending on the initial time lag Δ_a or Δ_b. (c) Voltage values and times to the section $\{v = V_0\}$ for cell 1 when cell 2 reaches the section $\{v = V_0\}$, with inhibition included, depending on the initial time lag Δ_a or Δ_b.

Lemma 2:

$$|\Delta_a - \Delta_b| < |\delta_a - \delta_b|. \tag{24}$$

Remark: Letting $\Delta_b \to \Delta_a$, this Lemma implies that $|\Pi'(\Delta_a)| > 1$, as desired. Note that the left and right sides of Eq. (24) correspond to the time metrics between the initial and final positions of v_a and v_b, respectively.

Proof: We follow the cells around in the phase plane until cell 1 returns to its initial position. Note that the evolution of cell 1 depends on whether the initial position of v_2 is at v_a or v_b. Let $(v_{1a}(t), n_{1a}(t))$ or $(v_{1b}(t), n_{1b}(t))$ be the positions of cell 1 if the initial position of v_2 is at v_a or v_b, respectively (Figure 14(a)). After cell 1 reaches threshold and fires, it returns to near Γ_0 and evolves along Γ_0 until cell 2 fires. Assume that $v_a(t)$ and $v_b(t)$ reach threshold at $t = T(\Delta_a)$ and $t = T(\Delta_b)$, respectively. Note that since $v_b(0) < v_a(0)$, it follows that $T(\Delta_b) > T(\Delta_a)$ and, therefore, $v_{1b}(T(\Delta_b)) > v_{1a}(T(\Delta_a))$. Moreover, using Lemma 1 and the fact that cell 1 follows the same trajectory along Γ_0 until cell 2 fires, we conclude that the time metric from $v_{1a}(T(\Delta_a))$ to $v_{1b}(T(\Delta_b))$ is $T(\Delta_b) - T(\Delta_a) > \Delta_b - \Delta_a$ (see Eq. (21) and Figure 14(b)).

Once either (v_a, n_a) or (v_b, n_b) fires, cell 1 turns around with $v_1' < 0$ until cell 2 falls below threshold, after which cell 1 returns to near Γ_0. As in the proof of Lemma 1, this causes a delay in how long it takes cell 1 to return to its initial position at $v = V_0$. Since $v_{1a}(T(\Delta_a)) < v_{1b}(T(\Delta_b))$, one can show, as in the proof of Lemma 1, that the delay for v_{1a} is greater than the delay for v_{1b}. More precisely, suppose that the time it would take cell 1 to go from $v_{1b}(T(\Delta_b))$ to V_0 if there was no inhibition is λ_b (Figure 14(b)). With inhibition, the time it takes v_{1b} to reach V_0 is $t_2(\Delta_b) - T(\Delta_b)$ (Figure 14(c)). Hence, the delay for v_{1b} is $t_2(\Delta_b) - T(\Delta_b) - \lambda_b$. On the other hand, if there is no inhibition, then the time it takes v_{1a} to reach V_0 is $\lambda_b + T(\Delta_b) - T(\Delta_a)$ and with inhibition the time it takes v_{1a} to reach V_0 is $t_2(\Delta_a) - T(\Delta_a)$ (Figures 14(b) and 14(c)). Hence, the delay for v_{1a} is $t_2(\Delta_a) - T(\Delta_b) - \lambda_b$. Since the delay for v_{1a} is greater than the delay for v_{1b}, we conclude that

$$t_2(\Delta_b) < t_2(\Delta_a). \tag{25}$$

Finally, note that the time metric between the final positions of v_b and v_a is

$$\delta_b - \delta_a = (t_2(\Delta_a) - T(\Delta_a)) - (t_2(\Delta_b) - T(\Delta_b)). \tag{26}$$

Applying Eq. (25) and Lemma 1 to Eq. (26), we conclude that

$$\delta_b - \delta_a > T(\Delta_b) - T(\Delta_a) > \Delta_b - \Delta_a > 0.$$

Thus, we have shown that Eq. (24) holds and the proof of the Lemma, and hence of the instability of the antiphase solution, is complete. □

This analysis demonstrates that a key ingredient determining the instability of the antiphase solution is the activation of the sodium current. In particular, formula (23) suggests that in order for the antiphase solution to be unstable, the parameter σ_m must be sufficiently large. In order to confirm whether this is indeed the case, we computed the second iterate of the reduced map; the antiphase solution corresponds to a fixed point of this second iterate map and one can determine the stability of the antiphase solution by computing the derivative of the second iterate map at this fixed point. In Figure 15(A), we plot the second iterate map for different values of σ_m. Note that the antiphase solution is stable for $\sigma_m = 9, 9.25$ and 9.5; however, it is unstable for $\sigma_m = 9.75$ and 10, consistent with our analysis. In Figure 15(b), we fix $\sigma_m = 9$ and vary g_{syn}. As expected, the antiphase solution is stable if g_{syn} is sufficiently small (less than approximately 0.4), but the antiphase solution becomes unstable and chaotic dynamics emerge for sufficiently large (but not too large) values of g_{syn}. We note that simulations of the map predict that the antiphase solution is always unstable for the default value of $\sigma_m = 10$.

VI. DEPENDENCE ON PARAMETERS AND LARGER NETWORKS

The analysis of the one-dimensional map, Π, in Sec. IV identifies key parameters that affect the stability of synchronous solutions of model (1). In this section, we systematically vary these parameters and compute the map numerically, using MATLAB, XPPAUT (http://www.pitt.edu/~phase), and Snnet.[40] In particular, we focus on the strength and decay rate of synaptic inhibition (g_{syn}, β), the reversal potential of

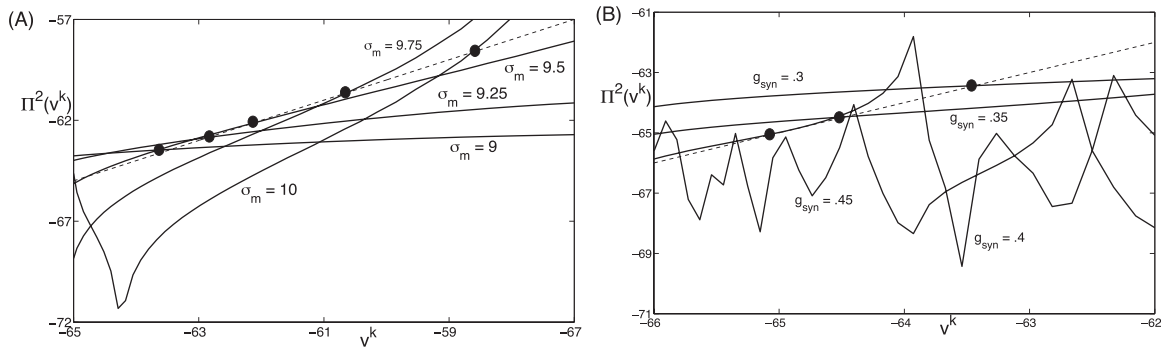

FIG. 15. Stability of the antiphase solution. (a) The second iterate of the reduced map (which we denote as $\Pi^2(v^k)$) for different values of σ_m. The antiphase solutions correspond to fixed points of these maps, illustrated with small circles along the fixed-point line (dashed). Note that the antiphase solution is unstable if the derivative of this map has absolute value greater than one at the fixed point. (b) The second iterate of the reduced map for different values of g_{syn} with $\sigma_m = 9$. Note that chaotic dynamics emerges when $g_{syn} = .45$ and it is not clear which fixed point corresponds to the antiphase solution in that case.

the leak current (v_L), and the slope of the sodium current activation curve (σ_m). We demonstrate that parameter choices for which the map predicts expansion of synchronous solutions lead to irregular activity in simulations of two-cell and 100-cell networks.

We compute a reduced map as described previously for Figure 3(c), with default parameter values $g_{syn} = 0.2$, $\beta = 1.0$, $v_L = -30$, and $\sigma_m = 10$. The derivative of the map at the synchronous solution, $\Pi'(0)$, is estimated as the slope of a line fit to the points of the map for which $-67.1 < v^k < -66.9$. The top row of Figure 16 shows how $\Pi'(0)$ changes as each parameter is varied individually, starting from the default values. The synchronous solution starts off unstable, i.e., $|\Pi'(0)| > 1$, and remains so until $g_{syn} \leq 0.13$, $\beta \geq 1.6$, or $v_L \geq -6$. The stability of the synchronous solution is evident in cross-correlograms constructed from 2-cell network simulations with parameter values chosen so that $|\Pi'(0)| < 1$ (middle row of Figure 16). The cross-correlograms with $g_{syn} = 0.1$, $\beta = 2.5$, or $v_L = 0$ have large peaks at a time shift of zero milliseconds, indicating synchronous spiking of the two cells. When these parameters are instead chosen so that $|\Pi'(0)| > 1$ (bottom row of Figure 16), the relative lack of structure in the cross-correlograms indicates that the synchronous solution is not stable. The corresponding irregular firing pattern is consistent with the expansion predicted by our analyses.

Over the range of σ_m values considered here (see the top right panel of Figure 16), $|\Pi'(0)| > 1$ and so the synchronous solution is always unstable. The cross-correlogram with $\sigma_m = 9.5$ (middle right panel of Figure 16) has symmetric peaks centered around, but not at, a time shift of zero milliseconds. This structure indicates that the antiphase solution is stable, as predicted by analysis of the second iterate map shown in Figure 15(a). When $\sigma_m = 10.5$ (bottom right panel of Figure 16), both the synchronous and antiphase solutions are unstable and the cross-correlogram reflects irregular firing of the two cells.

The ability of synaptic inhibition to induce uncorrelated spiking activity is even more evident in simulations of larger networks. Typical measures of uncorrelated activity in spike time recordings from the basal ganglia and prefrontal cortex include a lack of cross-correlations in spike times, exponentially distributed interspike intervals (ISIs), and ISI coefficients of variation (CVs) near unity. These characteristics are exhibited by five randomly chosen cells from a 100-cell network simulation (see Figure 17).

We also note that a relationship between irregular firing and g_{syn} is still detectable in the presence of voltage noise. Stochastic simulations of two-cell networks were performed using the Euler-Maruyama method. As g_{syn} is increased from 0 to 0.2, the autocorrelation in spike times decreases, indicating an increase in irregular activity (top row of Figure 18). However, after a certain point, further increasing g_{syn} (e.g., from 0.3 to 0.5) decreases irregularity (bottom row of Figure 18). In the deterministic system, $g_{syn} = 0.5$ gives a suppressed solution where only one cell fires.

VII. DISCUSSION

We have presented a Hodgkin-Huxley-type conductance-based model for inhibitory networks that exhibits irregular, uncorrelated activity patterns. The model is minimal in the sense that it contains only those currents required for irregular dynamics. However, this behavior also arises in other more complex Hodgkin-Huxley-like equations, such as the Wang-Buzsaki and Destexhe-Paré models,[29,30] which share features underlying the chaotic behavior in the model we consider.

By analyzing a one-dimensional map, we were able to derive rather precise conditions on parameters for when chaotic dynamics emerges in the two-cell network. In particular, the analysis yields explicit formulas for the derivative of the map at points corresponding to both the synchronous and the antiphase solutions. The full map was defined as the composition of three separate maps, each determining the dynamics of the solution during different portions of its trajectory through phase space. Interestingly, different parameters control the expansion of solutions during different portions of the cells' trajectories. In particular, during the spike, expansion depends on the strength, g_{syn} and decay rate, β, of synaptic inhibition. During the most hyperpolarized portion of the cells' trajectories, expansion depends on the interplay between the decay of synaptic inhibition and the decay of potassium activation. Finally, during the recovery phase, expansion depends primarily on the leak current and the activation of the sodium current.

Chaotic dynamics typically requires three ingredients: expansion, folding, and contraction.[34,35,41] In our model, as

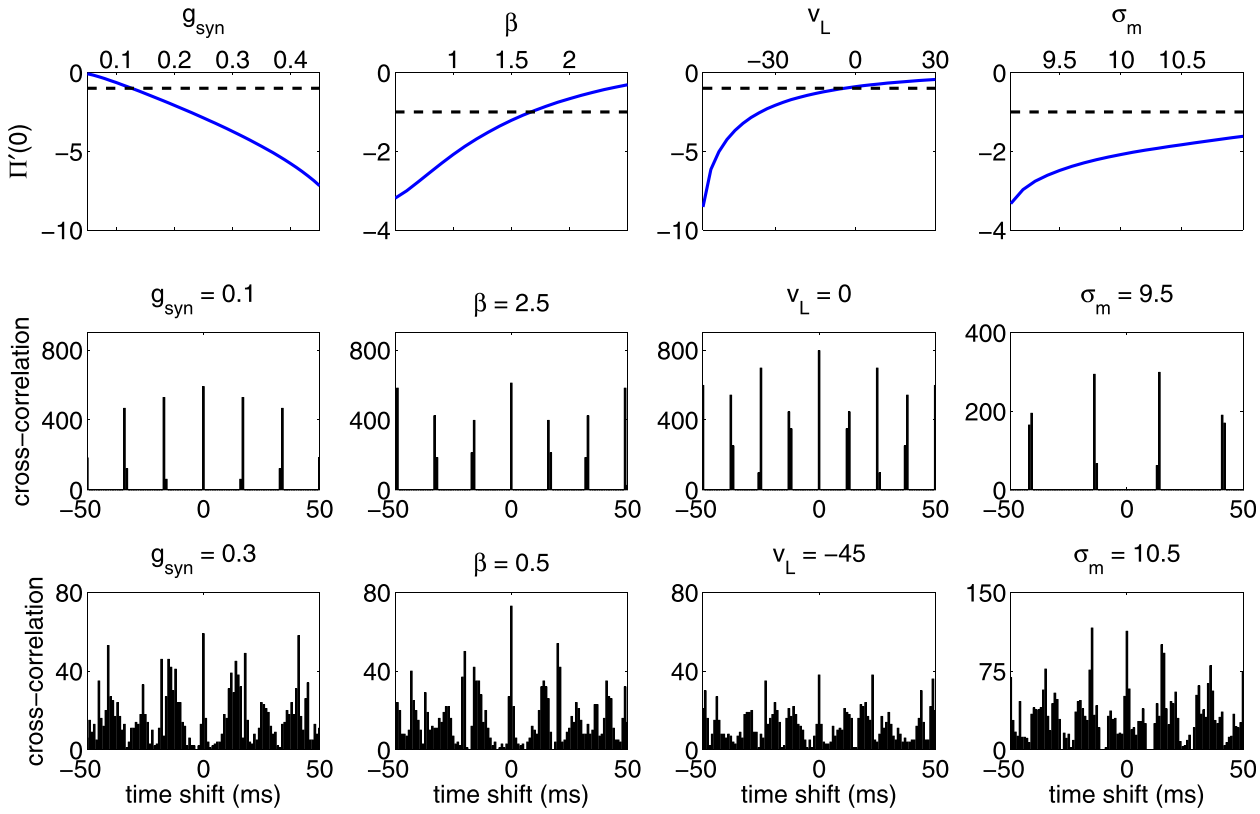

FIG. 16. Parameter dependence of the stability of the synchronous solution for 2-cell networks. Spike times are based on 60 s of simulation after discarding an initial 1 s transient. Parameter settings are $g_{syn} = 0.2$, $\beta = 1.0$, $v_L = -30$, and $\sigma_m = 10$ unless indicated otherwise. Top row: The slope of the reduced map shows that the synchronous solution goes from stable ($|\Pi'(0)| < 1$) to unstable ($|\Pi'(0)| > 1$) as g_{syn} is increased, as β is decreased, or as v_L becomes more hyperpolarized. Synchronous solution is unstable for all σ_m values shown. Dashed black lines indicates $|\Pi'(0)| = 1$. Middle row: Cross-correlograms corresponding to synchronous spiking for $g_{syn} = 0.1$, $\beta = 2.5$, and $v_L = 0$, and antiphase spiking for $\sigma_m = 9.5$. Bottom row: Cross-correlograms corresponding to irregular spiking.

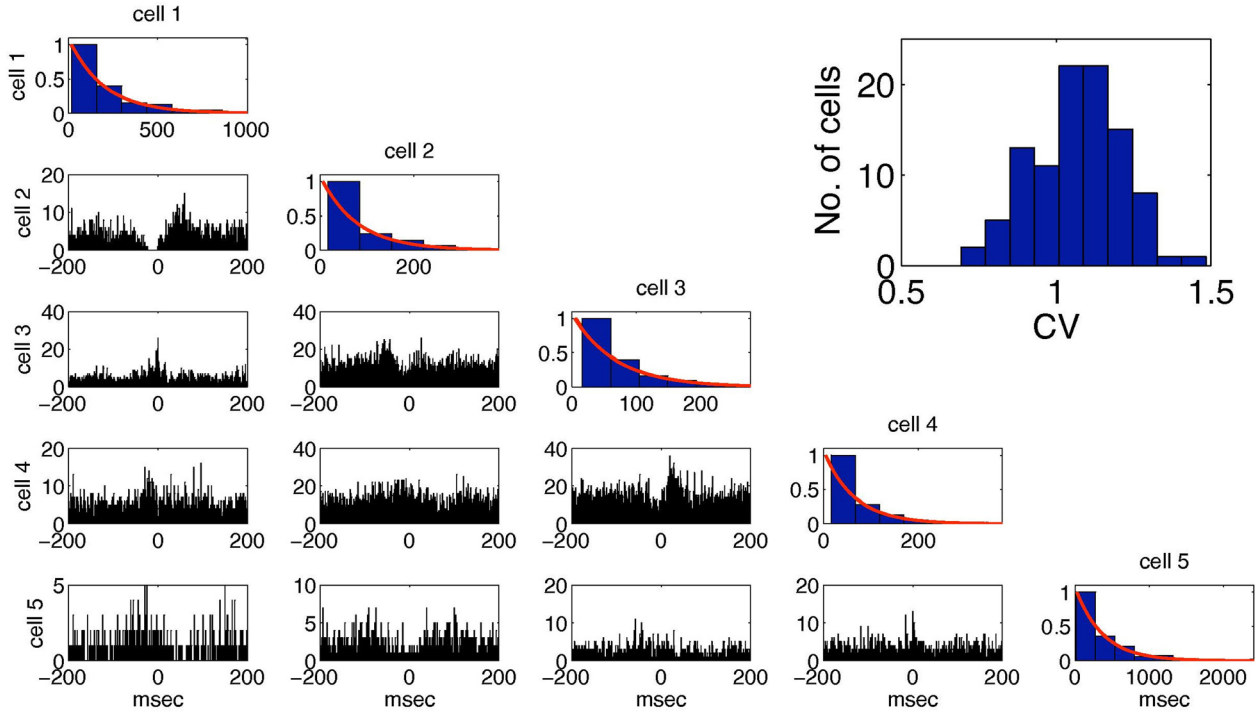

FIG. 17. Irregular spiking activity in a 100-cell inhibitory network simulation with 10% random connectivity, $g_{syn} = 1.0$, $\beta = 1.0$, $v_L = -30$, and $\sigma_m = 10$. Top right: Histogram of interspike interval coefficients of variation ($CV = \sigma_{ISI}/\mu_{ISI}$). CVs near one are typical of irregular activity in the prefrontal cortex. Diagonal: Histograms of ISIs for five randomly chosen cells with exponential fits (red lines) overlaid. Lower left: Pairwise cross-correlations in spike times between the five cells. Flat cross-correlograms are associated with irregular (non-parkinsonian) activity in the basal ganglia and in other neuronal networks.

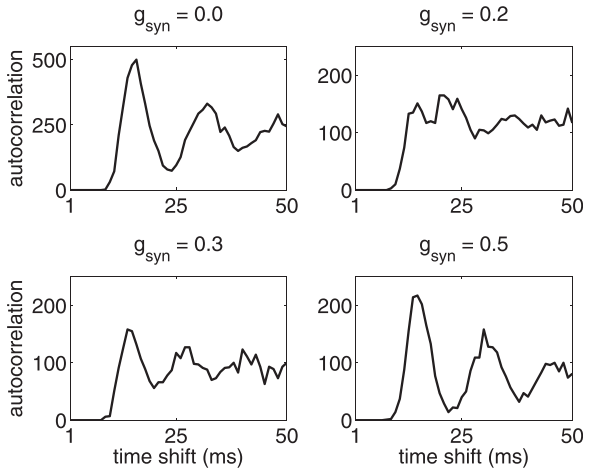

FIG. 18. Non-monotonic relationship between g_{syn} and irregular firing. Normal random variables ($\mu = 0$, $\sigma = 1$) were scaled by the square root of the Euler time step ($dt = 0.005$) and added to the right hand side of the voltage equation in simulations of model (1). Autocorrelation decreases from $g_{syn} = 0$ to 0.2, but increases from $g_{syn} = 0.3$ to 0.5.

described above, expansion between trajectories arises during both the spiking and hyperpolarized portions of each cycle. This expansion is due to differences in the synaptic inputs that the two cells receive as they traverse certain regions of the (v, n) phase space and occurs as long as the ratio of the rates at which the synapse decays and the potassium current deactivates is in an appropriate range. Additional expansion can also happen during the recovery phase due to properties of sodium activation. A form of folding also results from these effects, in that differences in timing of inhibition to the two cells can cause the leading cell to experience more potassium activation than the trailing cell, which causes the leading cell to become more hyperpolarized than the trailing cell and thus fall behind. Another form of folding arises each time a new inhibitory input impacts a recovering cell and causes its trajectory to fold back to more hyperpolarized voltages. Due to these folding effects, the cells may take turns firing on some cycles, while during other time periods, a cell may fire two or more spikes while the other cell remains silent; in terms of the map Π, if $\Delta > 0$, then it is possible for either $\Pi(\Delta) > 0$ or $\Pi(\Delta) < 0$ to result. We note that a contribution of such orientation switching to irregularity has been noted previously,[42] but there it occurred in transient activity in a large network, integrate-and-fire setting that is very different to what we have studied. Finally, contraction arises in our model because trajectories corresponding to each cell must approach very close to the synchronous trajectory, Γ_0, during the recovery phase (the Π_3 component of the map). This contraction preserves any expansion between trajectories that occurs in earlier parts of the cycle.

There have been numerous previous studies of reciprocal synaptic inhibition between spiking neurons.[33] These studies often considered reduced models, and they provided important insights into how the intrinsic and synaptic properties of the neurons involved interact to generate a variety of phase-locked states, including synchronous firing, antiphase behavior and almost in-phase oscillations.[33] It is not clear, however, how these previous reduced models can generate the robust uncorrelated dynamics that we have described. For example, in models based on relaxation oscillators, the jump up and jump down between the silent and active phases correspond to nearly horizontal trajectory paths in the (v, n) phase plane. For this reason, two cells coupled by inhibition must always maintain their orientation as they move around in phase space and it is not at all clear how the "folding" required for chaotic behavior can arise in these models. Other papers have considered integrate-and-fire type models, which typically ignore the dynamics of the spike and subsequent repolarization, two ingredients that we have demonstrated are essential for irregular spiking activity. We note that previous studies have demonstrated that the properties of spikes can contribute to the existence and stability of phase-locked activity patterns.[43,44]

The stability of phase-locked patterns in coupled networks has also been studied using the phase resetting curve (PRC).[33] Although this approach was initially developed to analyze models with weak coupling, several authors have extended the PRC method to cases in which the coupling is not weak.[38,45] In particular, our results complement and extend those of previous papers that have used PRC methods to study phase-locked solutions of mutually coupled inhibitory neurons in which there are alternations in the firing order of the two cells. Maran and Canavier[38] considered a network of heterogeneous Wang-Buzsaki model neurons[29] with type-I excitability[33] and demonstrated the emergence of 2:2 phase-locked states in which the firing order changes every cycle. Oh and Matveev[39] extended these results to show that alternating-order firing (sometimes called *leap-frog spiking*) may arise in a general class of inhibitory networks of type-I oscillators, as is the case for the model considered here. Using phase-plane methods, similar to those used in this paper, they noted that the alternating firing is closely related to the fast kinetics of K^+channels relative to the rate of change of the membrane potential during the quiescent phase of a cell's trajectory. As shown in Figure 1, this is the case for our model. Both of these earlier papers showed numerically that chaotic dynamics can arise for moderate levels of the synaptic coupling strength. Here, we study the chaotic dynamics analytically and derive precise conditions on parameters for when such dynamics exist. In order to use the PRC approach described in the previous papers,[38,39] one needs to compute a phase-resetting curve (or spike-time response curve) over a range of values of g_{syn}. Moreover, the analysis of phase-locked states reduces to finding a fixed point of a possibly large system of algebraic equations; the stability analysis consists of computing roots of a corresponding characteristic equation. Here, we have reduced the full dynamics to a single 1-dimensional map and we have made no assumptions on the firing order of the two cells.

To define the one dimensional reduced map, we needed to assume that the synaptic variables decay very close to zero during consecutive action potentials. For this reason, we chose the synaptic decay rate, $\beta = 1\, msec^{-1}$, to be sufficiently large. However, inhibitory $GABA_A$ synapses decay at a significantly slower rate. Numerical simulations with $\beta = .18\, msec^{-1}$ demonstrate that the assumption that the synaptic variables decay sufficiently between consecutive action potentials is no longer

valid, and one can no longer define the one-dimensional map. However, the simulations also demonstrate that in this case, the dynamics appears to be even more complex, so other mechanisms leading to chaotic behavior come into play. This would be an interesting issue to consider in future studies.

Irregular activity has also been considered in other types of networks, including those based on recurrent excitation and excitatory-inhibitory interactions. For example, theoretical analysis has established conditions for stability of the asynchronous state in these other types of networks; however, this analysis has been done for very large networks with sparse coupling.[23–28] Moreover, these studies do not elucidate how the intrinsic properties of the neurons' ionic currents contribute to irregular dynamics. An effect that has been found to produce irregular activity in a reciprocally connected pair of model neurons is shear-induced chaos.[41,46] Like the mechanisms we have analyzed, shear-induced chaos involves perturbation from an underlying oscillation and yields dynamics not predicted from the infinitesimal PRC. The phenomenon we study differs from that considered in these previous studies in several ways, however. In our system, the mechanisms that conspire to produce irregularity are distributed in a complex way over the extent of an oscillation, the perturbations are generated from within the system itself rather than being applied externally, the perturbing inputs do not turn off instantaneously, and the resulting irregularity is robust over an interval of coupling strengths.

While uncorrelated neuronal activity has been observed in a variety of brain regions, mechanisms underlying this uncorrelated activity are poorly understood. A detailed analysis and classification of how uncorrelated and irregular activity patterns can arise in a general class of biologically-based model networks may be very useful for understanding the origins of uncorrelated firing in some of these brain areas and for interventions aimed at switching firing patterns there. For example, uncorrelated activity occurs under normal resting conditions in the inhibitory globus pallidus network in the basal ganglia. In parkinsonian states in which dopamine are depleted within the basal ganglia, however, such activity is replaced by significantly more correlated firing.[1,2,5–7] A variety of experiments have demonstrated that dopamine may have multiple effects on the firing properties of neurons within these nuclei. In particular, dopamine may alter the strengths of their inhibitory synapses[47–50] and may modulate the activation of certain sodium currents.[51] Our analysis shows that changing parameters in the model corresponding to each of these processes may switch the network activity between phase-locked spiking and uncorrelated states. The analysis we have presented may therefore offer useful insights into how parkinsonian conditions lead to abnormally high correlations in activity within the globus pallidus, which in turn could influence activity downstream from the globus pallidus and throughout the basal ganglia-thalamo-cortical network.[52–54]

ACKNOWLEDGMENTS

This work was partially supported by the National Science Foundation DMS Award Nos. 1021701, 1312508 (JR), 1022627 (DT) and 0931642 (Mathematical Biosciences Institute). We thank the Department of Mathematics at the University of Auckland for its hospitality during part of the completion of this work.

[1]A. Nini, A. Feingold, H. Slovin, and H. Bergman, "Neurons in the globus pallidus do not show correlated activity in the normal monkey, but phase-locked oscillations appear in the MPTP model of parkinsonism," J. Neurophysiol. **74**, 1800–1805 (1995).
[2]A. Raz, E. Vaadia, and H. Bergman, "Firing patterns and correlations of spontaneous discharge of pallidal neurons in the normal and the tremulous 1-methyl-4-phenyl-1,2,3,6-tetrahydropyridine vervet model of parkinsonism," J. Neurosci. **20**, 8559–8571 (2000).
[3]I. Bar-Gad, G. Heimer, Y. Ritov, and H. Bergman, "Functional correlations between neighboring neurons in the primate globus pallidus are weak or nonexistent," J. Neurosci. **23**, 4012–4016 (2003).
[4]G. Heimer, M. Rivlin-Etzion, I. Bar-Gad, J. A. Goldberg, S. N. Haber, and H. Bergman, "Dopamine replacement therapy does not restore the full spectrum of normal pallidal activity in the 1-methyl-4-phenyl-1,2,3,6-tetra-hydropyridine primate model," J. Neurosci. **26**, 8101–8114 (2006).
[5]H. Bergman, A. Feingold, A. Nini, A. Raz, H. Slovin, M. Abeles, and E. Vaadia, "Physiological aspects of information processing in the basal ganglia of normal and parkinsonian primates," Trends Neurosci. **21**, 32–38 (1998).
[6]J. Hurtado, C. Gray, L. Tamas, and K. Sigvardt, "Dynamics of tremor-related oscillations in the human globus pallidus," Proc. Nat. Acad. Sci. USA **96**, 1674–1679 (1999).
[7]J. T. Gale, R. Amirnovin, Z. M. Williams, A. W. Flaherty, and E. N. Eskandar, "From symphony to cacophony: Pathophysiology of the human basal ganglia in Parkinson disease," Neurosci. Biobehav. Rev. **32**, 378–387 (2008).
[8]S. Funahashi, C. J. Bruce, and P. S. Goldman-Rakic, "Mnemonic coding of visual space in the monkey's dorsolateral prefrontal cortex," J. Neurophysiol. **61**, 331–349 (1989).
[9]J. Quintana and J. M. Fuster, "From perception to action: temporal integrative functions of prefrontal and parietal neurons," Cereb. Cortex **9**, 213–221 (1999).
[10]G. Rainer, W. F. Asaad, and E. K. Miller, "Selective representation of relevant information by neurons in the primate prefrontal cortex," Nature **393**, 577–579 (1998).
[11]A. Compte, "Computational and in vitro studies of persistent activity: edging towards cellular and synaptic mechanisms of working memory," Neuroscience **139**, 135–151 (2006).
[12]F. Barbieri and N. Brunel, "Can attractor network models account for the statistics of firing during persistent activity in prefrontal cortex?," Front. Neurosci. **2**, 114–122 (2008).
[13]K. Negishi, E. S. Lu, and M. Verzeano, "Neuronal activity in the lateral geniculate body and the nucleus reticularis of the thalamus," Vision Res. **1**, 343–353 (1962).
[14]Y. Lamarre, M. Filion, and J. Cordeau, "Neuronal discharges of the ventrolateral nucleus of the thalamus during sleep and wakefulness in the cat i. spontaneous activity," Exp. Brain Res. **12**, 480–498 (1971).
[15]U. Büttner, V. Henn, and H. Oswald, "Vestibular–related neuronal activity in the thalamus of the alert monkey during sinusoidal rotation in the dark," Exp. Brain Res. **30**, 435–444 (1977).
[16]M. Steriade, D. A. McCormick, and T. J. Sejnowski, "Thalamocortical oscillations in the sleeping and aroused brain," Science **262**, 679–685 (1993).
[17]S. Kim, J. Jeong, Y. Kwak, Y. Kim, S. Jung, and K. Lee, "Fractal stochastic modeling of spiking activity in suprachiasmatic nucleus neurons," J. Comput. Neurosci. **19**, 39–51 (2005).
[18]J. Jeong, Y. Kwak, Y. Kim, and K. Lee, "Dynamical heterogeneity of suprachiasmatic nucleus neurons based on regularity and determinism," J. Comput. Neurosci. **19**, 87–98 (2005).
[19]C. Diekman and D. Forger, "Clustering predicted by an electrophysiological model of the suprachiasmatic nucleus," J. Biol. Rhythms **24**, 322–333 (2009).
[20]G. Freeman, R. Krock, S. Aton, P. Thaben, and E. Herzog, "Gaba networks destabilize genetic oscillations in the circadian pacemaker," Neuron **78**, 799–806 (2013).
[21]A. Renart, J. de la Rocha, P. Bartho, L. Hollender, N. Parga, A. Reyes, and K. D. Harris, "The asynchronous state in cortical circuits," Science **327**, 587–590 (2010).

[22]T. Tetzlaff, M. Helias, G. T. Einevoll, and M. Diesmann, "Decorrelation of neural-network activity by inhibitory feedback," PLOS Comput. Biol. **8**, e1002596 (2012).
[23]L. Abbott and C. van Vreeswijk, "Asynchronous states in networks of pulse-coupled neurons," Phys. Rev. E **48**, 1483–1490 (1993).
[24]M. Tsodyks and T. Sejnowski, "Rapid state switching in balanced cortical network models," Network Comput. Neural Syst. **6**, 111–124 (1995).
[25]C. van Vreeswijk and H. Sompolinsky, "Chaos in neuronal networks with balanced excitatory and inhibitory activity," Science **274**, 1724–1726 (1996).
[26]N. Brunel, "Dynamics of sparsely connected networks of excitatory and inhibitory spiking neurons," J. Comput. Neurosci. **8**, 183–208 (2000).
[27]W. Gerstner, "Population dynamics of spiking neurons: fast transients, asynchronous states, and locking," Neural Comput. **12**, 43–89 (2000).
[28]T. P. Vogels, K. Rajan, and L. Abbott, "Neural network dynamics," Annu. Rev. Neurosci. **28**, 357–376 (2005).
[29]X. J. Wang and G. Buzsaki, "Gamma oscillation by synaptic inhibition in a hippocampal interneuronal network model," J. Neurosci. **16**, 6402–6413 (1996).
[30]A. Destexhe and D. Paré, "Impact of network activity on the integrative properties of neocortical pyramidal neurons in vivo," J. Neurophysiol. **81**, 1531–1547 (1999).
[31]A. Hodgkin and A. Huxley, "A quantitative description of membrane current and its application to conduction and excitation in nerve," J. Physiol. (London) **117**, 500–544 (1952).
[32]G. B. Ermentrout and J. Rinzel, "Differential equations," *in Computational Modeling Methods for Neuroscientists*, edited by E. De Schutter (The MIT Press, Cambridge, MA, 2010).
[33]G. B. Ermentrout and D. H. Terman, *Mathematical Foundations of Neuroscience* (Springer-Verlag New York, 2010), Vol. 35.
[34]J. Guckenheimer and P. Holmes, *Nonlinear Oscillations, Dynamical Systems, and Bifurcations of Vector Fields* (Springer–Verlag New York, 1983), Vol. 42.
[35]R. Devaney, *An Introduction to Chaotic Dynamical Systems* (Westview Press, Boulder, CO, 2003).
[36]A. Wolf, J. Swift, H. Swinney, and J. Vastano, "Determining lyapunov exponents from a time series," Physica D **16**, 285–317 (1985).
[37]V. Govorukhin, see http://http://www.math.rsu.ru/mexmat/kvm/matds, for Matds (2004).
[38]S. K. Maran and C. C. Canavier, "Using phase resetting to predict 1:1 and 2:2 locking in two neuron networks in which firing order is not always preserved," J. Comput. Neurosci. **24**, 37–55 (2008).
[39]M. Oh and V. Matveev, "Loss of phase-locking in non-weakly coupled inhibitory networks of type-I model neurons," J. Comput. Neurosci. **26**, 303–320 (2009).
[40]R. McDougal, see http://senselab.med.yale.edu/simtooldb/showtool.asp?tool=144396 for Snnet (2011).
[41]L.-S. Young, "Understanding chaotic dynamical systems," Commun. Pure Appl. Math. **66**, 1439–1463 (2013).
[42]R. Zillmer, R. Livi, A. Politi, and A. Torcini, "Desynchronization in diluted neural networks," Phys. Rev. E **74**, 036203 (2006).
[43]C. Chow and N. Kopell, "Dynamics of spiking neurons with electrical coupling," Neural Comput. **12**, 1643–1678 (2000).
[44]S. Jalil, I. Belykh, and A. Shilnikov, "Spikes matter for phase-locked bursting in inhibitory neurons," Phys. Rev. E **85**, 036214 (2012).
[45]P. Goel and B. Ermentrout, "Synchrony, stability, and firing patterns in pulse-coupled oscillators," Physica D **163**, 191–216 (2002).
[46]K. Lin, E. Shea-Brown, and L. Young, "Reliability of coupled oscillators," J. Nonlinear Sci. **19**, 497–545 (2009).
[47]K. Shen and S. Johnson, "Presynaptic dopamine D2 and muscarine M3 receptors inhibit excitatory and inhibitory transmission to rat subthalamic neurones in vitro," J. Physiol. (London) **525**, 331–341 (2000).
[48]S. Cragg, J. Baufreton, Y. Xue, J. Bolam, and M. Bevan, "Synaptic release of dopamine in the subthalamic nucleus," Eur. J. Neurosci. **20**, 1788–1802 (2004).
[49]K. Shen and S. Johnson, "Dopamine depletion alters responses to gluatamate and GABA in the rat subthalamic nucleus," Neuroreport **16**, 171–174 (2005).
[50]C. J. Wilson and M. D. Bevan, "Intrinsic dynamics and synaptic inputs control the activity patterns of subthalamic nucleus neurons in health and in parkinson's disease," Neuroscience **198**, 54–68 (2011).
[51]D. C. Rotaru, D. A. Lewis, and G. Gonzalez-Burgos, "Dopamine d1 receptor activation regulates sodium channel-dependent epsp amplification in rat prefrontal cortex pyramidal neurons," J. Physiol. **581**, 981–1000 (2007).
[52]Y. Guo, J. E. Rubin, C. C. McIntyre, J. L. Vitek, and D. Terman, "Thalamocortical relay fidelity varies across subthalamic nucleus deep brain stimulation protocols in a data-driven computational model," J. Neurophysiol. **99**, 1477–1492 (2008).
[53]P. Reitsma, B. Doiron, and J. E. Rubin, "Correlation transfer from basal ganglia to thalamus in parkinson's disease," Front. Comput. Neurosci. **5**, Art. 58 (2011).
[54]J. E. Rubin, C. C. McIntyre, R. S. Turner, and T. Wichmann, "Basal ganglia activity patterns in parkinsonism and computational modeling of their downstream effects," Eur. J. Neurosci. **36**, 2213–2228 (2012).